A macroscopic damage-plastic constitutive law for modelling quasi-brittle fracture and ductile behavior of concrete

P.J. Sánchez[†‡], A.E. Huespe[†], J. Oliver[♯], G. Diaz[♯], and V.E. Sonzogni[†]

† CIMEC-INTEC-UNL-CONICET, Güemes 3450, 3000 Santa Fe, Argentina.

♯ ETSECCP, Technical University of Catalonia, Barcelona, Spain.

‡ GIMNI-UTN-FRSF, Lavaisse 610, 3000 Santa Fe, Argentina.

Abstract: A new phenomenological macroscopic constitutive model for the numerical simulation of quasi-brittle fracture and ductile concrete behavior, under general triaxial stress conditions, is presented. The model is particularly addressed to simulate a wide range of confinement stress states, as also, to capture the strong influence of the mean stress value in the concrete failure mechanisms.

The model is based on a two-surface damage-plastic formulation. The mechanical behavior in different domains of the stress space is separately described by means of a *quasi-brittle* or *ductile* material response:

(i) For positive values of the mean stress (tensile states), an isotropic continuum damage model with strain softening is considered. In this context, and in order to avoid the *Boundary Value Problem* ill-posedness induced by the softening law, a regularization technique based on the *Continuum Strong Discontinuity Approach* (*CSDA*) is adopted, which results equivalent to a damage model with embedded cohesive cracks.

(ii) A plastic model governs the material behavior when the mean stress is negative (confinement states). It is based on the classical plastic flow theory. In particular, a yield criterion similar to that of Willam and coauthors, which depends on the three stress invariants, is used. Additional features defining the plastic response are: an isotropic strain hardening law and a non-associative flow rule.

The paper presents the numerical implementation of the model using an efficient integration algorithm, namely the *Im-plex* scheme. Several widely known experimental tests (such as: uni-axial, bi-axial and tri-axial tests) carried out on concrete specimens are used to calibrate and validate the performance of the proposed formulation. Finally, a classical 2D reinforced concrete beam example is analyzed in order to show the predictive capability of the model in structural analysis applications.

Keywords: concrete constitutive model, concrete fracture, quasi-brittle ductile failure, strong discontinuity approach.

1 Introduction

Plain and reinforced concrete (RC) structures are subjected to a diversity of loads during its service life. This requires, from the material modeling point of view, a sufficiently general description of the concrete response. Unfortunately, development of such a general model, useful in all these diverse load conditions, is not a trivial task. The concrete mechanical behavior is very complex, and the difficulty of its description increases enormously if material failure is considered (Kang et al., 2000; Kang, 1997). Indeed, this topic remains an open and very challenging issue in numerical simulations of, mainly, RC structures.

There are many experimental evidences showing that, depending on the stress state and more specifically on the stress confinement level (see Sfer et al. (2002)), the concrete failure modes change drastically. From highly localized failure modes, including singularities and discontinuities like fractures, cracks, etc., to smeared strain patterns, such as crushing zones where not visible macro cracks are present, can be observed in degraded concrete structures. In other words, the characteristic lengths where the material degradation phenomenon takes place, and so the dissipation mechanisms and the induced failure modes, are strongly dependent of the mean stress value.

Under tensile stresses, the concrete undergoes micro-cracking (even for relatively small stress values), strain softening and degradation of the elastic stiffness. In this regime, the inelastic deformations are practically negligible, displaying a much lower strength and a higher brittleness than in compressive states. Formation of cracks are expected only for tensile dominant states. The classical *Continuum Damage Mechanics* seems to be the rational constitutive framework to represent this material behavior (Lemaitre and Desmorat, 2005). However, due to the practically inexistent stage of stable damage evolution, it becomes mandatory to include a regularization technique in the model, in order to keep its response well-posed and objective.

Alternatively, for high confinement stress states, the material response displays noticeable inelastic deformations jointly with a very marked hardening behavior; unloading processes do not reveal a sensitive degradation of the elastic stiffness. In this case, the classical *Flow Theory of Plasticity* can be adopted as the underlying constitutive model (Lubliner, 1990).

The aforementioned phenomenology has motivated, in the last years, the formulation of many improved macroscopic constitutive theories coupling damage and plasticity, see for example the contributions of Etse and Willam (1994), Cervenka and Papanikolaou (2008), Winkler et al. (2001), Winkler et al. (2004), Luccioni and Rougier (2005), Grassl and Jirasek (2006), Pivonka et al. (2004), Feenstra and de Borst (1996), Contrafatto and Cuomo (2006), Meschke et al. (1998), among others. Even more, the complexities of the problem have stimulated the development of *micro* and *meso*-mechanics formulations (Mattei et al. (2007), Caballero et al. (2006)) and the present trend in material modeling suggests that the future research lines will be based on *multi-scale* formulations. The present article follows the first conceptual philosophy: a *macroscopic* or *phenomenological* approach to the material modeling of concrete, without considering the meso-structure, is addressed. Some specific features of the proposed model, and differences with respect to the previous documented ones, can be mentioned:

- A very simple and intuitive criterion, based on the mean stress value, is used for associating to concrete an inelastic response, which follows either a damage or a plastic regime, and so a *"quasi-brittle"* or *"ductile"* behavior can be captured.

- The proposed constitutive law has a reduced number of material parameters, most of them can be easily obtained from standard experimental tests, therefore the resultant concrete model is relatively simple to characterize.

- The evolution laws of the internal variable of each sub-model (damage or plasticity) are uncoupled.

- The intersection geometry, between both inelastic limit surfaces (damage and plasticity), turns out to be very simple (a circle located in the octahedral plane) and constant from the topological point of view. This feature facilitates the formulation of the return mapping schemes improving the robustness of the non-linear algorithm. In this context, the formulation and implementation of a very efficient integration strategy is also mentioned.

- A key ingredient of the model: the damage regime is based on an efficient and robust regularization technique which permits the nucleation and propagation of multiple tensile cracks in the medium due to the explicit incorporation of an enhanced kinematics with strong discontinuities. Specifically, we refer to the *Continuum Strong Discontinuity Approach (CSDA)*. In this contribution, only a brief summary of the damage model regularization is presented. Specific details of this issue are addressed in Oliver (2000); Oliver et al. (2002) and the bibliography cited therein.

- The model does not consider neither a failure criterion in exclusively confinement stress states (reasons for this strong simplifying assumption are given in the paper), nor cyclic loading.

- The use of anisotropic damage models for concrete has been widely justified in many articles. Even though the proposed continuum damage model for the *stable* quasi-brittle mechanical response of concrete is, by definition, isotropic; this characteristic is drastically modified once the embedded strong discontinuity technique and the corresponding regularization method is introduced after the *material instability* detection (see Sub-section 2.1). The CSDA, as a regularization technique, induces a very marked anisotropic response, typical of concrete in tensile regimes, because it can be understood as a method for embedding directional cracks (an approach widely used by the scientific community in the context of numerical simulation of quasi-brittle failure, see for example Sancho et al. (2007); Gasser and Holzapfel (2005); Lotfi and Shing (1995). Finite elements with embedded cracks can be seen in the works of Mosler and Meschke (2004); Alfaiate et al. (2002); Jirásek (2000), Feist and Hofstetter (2006).

In summary, a relatively simple constitutive law which accounts for the more relevant macroscopic phenomenology in the concrete is presented. It is emphasized that the proposed model is specially useful for the numerical simulation of RC members where co-exist: *(i)* tensile stress domains with severe degradation, including crack

propagation, and *(ii)* zones with crushing induced by plasticity for confinement stress states. Both mechanisms govern the failure modes and the ultimate load carrying capacity for this type of structures.

The remaining part of the paper is structured as follows. In the next Section (Section 2), the mathematical formulation and the basic features of the proposed concrete model are described. The characterization of the material model parameters are discussed in Section 3. In Section 4, a robust and computationally efficient numerical algorithm for the integration of the constitutive equations is presented. A comparison between the obtained numerical simulations and experimental results for uni-axial, bi-axial and tri-axial tests are presented in Section 5. In fact, this section must be seen in a twofold sense: as a characterization of the parameters, and also, as a validation of the model. An application to one RC structure is shown in Section 6. Finally, the conclusions are presented in Section 7. Two Appendices include discussions about the minimal restrictions to be considered in the definition of the model parameters in order to guaranty thermodynamic consistency and convexity of the inelastic surfaces.

2 Concrete model description

The constitutive model for concrete is formulated in terms of a consistent coupling between an elasto-plastic law and a scalar damage law. Figure 1 displays a graphical representation, in the Haigh-Westergaard's stress space, of the proposed limit surfaces. The basic features of the model are discussed next:

- The fracture phenomenon, typical of tensile stress states, is described by an isotropic damage evolution law, similar to that proposed by Oliver (2000), and regularized by the *CSDA* methodology. Damage evolution is only possible when the mean stress is positive. In this case, the material softening induces instability and strain localization. This mechanism is the precursor for the initiation and propagation of cracks.
- In compressive stress regimes, negative mean stress, the concrete behaves like a plastic material following very closely the Willam's elasto-plastic model, see Willam and Warnke (1974) and Kang and Willam (1999). In this situation there is not damage evolution and the plastic model displays a very marked hardening regime. The plastic flow is non-associative, material stability cannot be guaranteed even for large hardening moduli. However, at least in all the present numerical simulations, no material bifurcation (i.e material instabilities) have been detected during the plastic regime.

In Table 1, the governing basic equations of the damage-plastic model are presented. The notation and some important observations are as follows:

- In equation (1), $\Psi = \Psi(\boldsymbol{\varepsilon}^e, d, \alpha)$ is the Helmholtz's free energy defined as the sum of two different contributions: an elastic-damage energy $\Psi^d(\boldsymbol{\varepsilon}^e, d)$, defined by:

$$\Psi^d(\boldsymbol{\varepsilon}^e, d) = \frac{1}{2}(1-d)\left[\boldsymbol{\varepsilon}^e : \mathbb{C}^e : \boldsymbol{\varepsilon}^e\right] \tag{16}$$

Helmholtz's free energy function:

$$\Psi(\boldsymbol{\varepsilon}^e, d, \alpha) = \Psi^d(\boldsymbol{\varepsilon}^e, d) + \Psi^p(\alpha) \tag{1}$$

$$\dot{\Psi} = \frac{\partial \Psi^d}{\partial \boldsymbol{\varepsilon}^e} : \dot{\boldsymbol{\varepsilon}}^e + \frac{\partial \Psi^d}{\partial d}\,\dot{d} + \frac{\partial \Psi^p}{\partial \alpha}\,\dot{\alpha} \tag{2}$$

Additive decomposition of strains:

$$\boldsymbol{\varepsilon} = \boldsymbol{\varepsilon}^e + \boldsymbol{\varepsilon}^p \tag{3}$$

Stress-Strain relationship:

$$\boldsymbol{\sigma} = (1-d)\,\mathbb{C}^e : \underbrace{(\boldsymbol{\varepsilon} - \boldsymbol{\varepsilon}^p)}_{\boldsymbol{\varepsilon}^e} = \frac{q}{r}\,\bar{\boldsymbol{\sigma}} \quad ; \qquad \mathbb{C}^e = \lambda\,(\mathbb{1}\otimes\mathbb{1}) + 2\,\mu\,\mathbb{I} \tag{4}$$

Brittle-Ductile behavior:

IF $\{(\sigma_m > 0)$ ***OR*** $(\sigma_m = 0\ \&\ tr(\mathbb{C}^e : \dot{\boldsymbol{\varepsilon}}) \geq 0)\}$ ***THEN***

Elastic-Damage model, possible evolution of variable"d" $(\dot{\boldsymbol{\varepsilon}}^p = \boldsymbol{0})$:

$$g(\boldsymbol{\varepsilon}, r) = \tau_\varepsilon - r \quad ; \quad \tau_\varepsilon = \sqrt{\boldsymbol{\varepsilon}^e : \mathbb{C}^e : \boldsymbol{\varepsilon}^e} = \sqrt{\bar{\boldsymbol{\sigma}} : (\mathbb{C}^e)^{-1} : \bar{\boldsymbol{\sigma}}} \tag{5}$$

$$\hat{g}(\boldsymbol{\sigma}, q) = \frac{q}{r}\,g(\boldsymbol{\varepsilon}) = \tau_\sigma - q \quad ; \quad \tau_\sigma = \sqrt{\boldsymbol{\sigma} : (\mathbb{C}^e)^{-1} : \boldsymbol{\sigma}} \tag{6}$$

$$\dot{r} = \gamma^d \quad ; \quad r|_{t=0} = r_0 = \frac{f_t}{\sqrt{E}} \quad (\gamma^d : \text{damage consistency parameter}) \tag{7}$$

$$\dot{q} = H(r)\,\dot{r} \quad ; \quad q|_{t=0} = q_0 = \frac{f_t}{\sqrt{E}} \tag{8}$$

$$\gamma^d \geq 0 \quad ; \quad \hat{g}(\boldsymbol{\sigma}, q) \leq 0 \quad ; \quad \gamma^d\,\hat{g}(\boldsymbol{\sigma}, q) = 0 \tag{9}$$

ELSE IF $\{(\sigma_m < 0)$ ***OR*** $(\sigma_m = 0\ \&\ tr(\mathbb{C}^e : \dot{\boldsymbol{\varepsilon}}) < 0)\}$ ***THEN***

Elasto-Plastic model, possible evolution of variable "$\boldsymbol{\varepsilon}^p$*"* $(\dot{d} = 0)$:

$$\psi(\boldsymbol{\sigma}, \xi) = \frac{1}{2}\,\hat{r}(e,\theta)\,\|\boldsymbol{S}\|^\beta + \xi(\alpha)\,\sigma_m - k_m \quad ; \quad k_m \in [0; k_{m\,max}] \tag{10}$$

$$\xi = \frac{\partial \Psi^p}{\partial \alpha}; \qquad \xi(\alpha) \in [\xi_0; \xi_{max}) \tag{11}$$

$$\dot{\boldsymbol{\varepsilon}}^p = \gamma^p\,\frac{\partial G}{\partial \boldsymbol{\sigma}} = \gamma^p\left[\frac{\beta}{2}\,\|\boldsymbol{S}\|^{\beta-1}\,\boldsymbol{n} + \chi\,\frac{\xi(\alpha)}{3}\,\mathbb{1}\right] \quad ; \quad \boldsymbol{n} = \boldsymbol{S}\,\|\boldsymbol{S}\|^{-1} \tag{12}$$

$$G(\boldsymbol{\sigma}, \xi) = \frac{1}{2}\,\|\boldsymbol{S}\|^\beta + \chi\,\xi(\alpha)\,\sigma_m - k_m \tag{13}$$

$$\dot{\alpha} = -\gamma^p\,\frac{\partial G}{\partial \xi} = -\gamma^p\,\chi\,\sigma_m \quad ; \quad \alpha|_{t=0} = 0 \quad (\gamma^p : \text{plastic multiplier}) \tag{14}$$

$$\gamma^p \geq 0 \quad ; \quad \psi(\boldsymbol{\sigma}, \xi) \leq 0 \quad ; \quad \gamma^p\,\psi(\boldsymbol{\sigma}, \xi) = 0 \tag{15}$$

END

Table 1: Basic equations and conceptual scheme of the Damage-Plastic model for concrete.

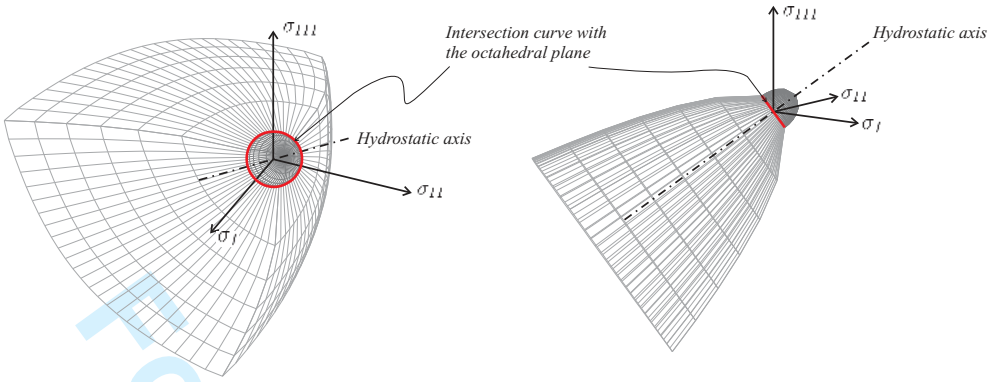

Figure 1: Damage-Plastic model: Representation of the limit surfaces in the Haigh-Westergaard's space of principal stresses.

and an energy function $\Psi^p(\alpha)$ which depends on the hardening mechanism in the plastic regime. In the present context, $\Psi^p(\alpha)$ is the potential function for the plastic hardening law, $\xi(\alpha)$, and it has the form:

$$\Psi^p(\alpha) = \int_{\alpha=0}^{\alpha=\alpha} \xi(\alpha)\, d\alpha = \int_{t=0}^{t=t} \xi(\alpha)\, \dot{\alpha}\, dt \tag{17}$$

where, $\boldsymbol{\varepsilon}^e$ is the elastic strain component, $\mathbb{C}^e$ is the fourth order isotropic elastic tensor and the internal variables d, ξ and α are explained in the following points. Equation (2), in Table 1, shows the rate expression of the Helmholtz's free energy function.

- The standard (scalar) damage variable "d" is defined as:

$$d(r) = 1 - \frac{q(r)}{r} \tag{18}$$

with r and q, the set of internal scalar variables for the damage model. The evolution laws of r and q are discussed next.

- $\{\boldsymbol{\varepsilon}^p, \alpha, \xi\}$ is the set of internal variables for the plasticity model, where $\boldsymbol{\varepsilon}^p$ represents the plastic component of the total strain tensor $\boldsymbol{\varepsilon}$ (see equation (3)), α is a monotonously increasing scalar variable, and the function ξ governs the hardening of the plastic process (its characterization is given in the next section).

- From the thermodynamic point of view, there is a duality relation between q and r, as well as, between ξ and α.

- In the first equation (4), $\boldsymbol{\sigma}$ is the Cauchy's stress, $\overline{\boldsymbol{\sigma}}$ is the effective stress associated with the damage model, which is defined by means of the elastic relation: $\overline{\boldsymbol{\sigma}} = \mathbb{C}^e : (\boldsymbol{\varepsilon} - \boldsymbol{\varepsilon}^p)$. In the right expression (4), the isotropic elastic tensor is defined. The symbols $\mathbb{1}$ and $\mathbb{I}$ are the second order identity tensor and the fourth order symmetric identity tensor, respectively; λ and μ are the Lame's parameters. We define: $\sigma_m = \frac{1}{3}\, tr(\boldsymbol{\sigma})$ as the mean stress and $\boldsymbol{S} = dev(\boldsymbol{\sigma}) = (\boldsymbol{\sigma} - \sigma_m \mathbb{1})$ as the deviatoric stress tensor.

- The concrete constitutive model in Table 1 is represented in two blocks accounting for: *i)* the *quasi-brittle* behavior described through a damage inelastic law (see equations (5)-(9)), or *ii)* the *ductile* behavior described through a plasticity law (see equations (10)-(15)). Decision of which inelastic mechanism evolves (damage or plasticity) only depends on the sign of the mean stress.

- Elastic-Damage model ($\sigma_m \geq 0$): "*quasi-brittle*" behaviour:

  - In tensile regimes, while the material is not completely degraded, it is verified that: $0 < \frac{q}{r} \leq 1$. Thus, the damage criterion is given by the surface $g(\boldsymbol{\varepsilon}, r) = 0$ or, alternatively, $\hat{g}(\boldsymbol{\sigma}, q) = 0$, see equations (5) and (6). Geometrically, this surface is an ellipsoid in the Haigh-Westergaard's space, see Figure 1 and 2-(a), which intersects the octahedral plane in a circle of radius: $R = \|\boldsymbol{S}\| = \sqrt{2\mu}\ q$. During damage evolution the variable $q \to 0$, and the circle radius tends to zero or equivalently the intersection curve shrinks to a point, see Figure 2-(d).

  - Equations (7) and (8) define the evolution laws for the damage internal variables r and q, respectively. Note that their initial values (r_0 and q_0) are also defined in those expressions which determines the initial damage value $d_0 = 0$. The term f_t is the uniaxial ultimate tensile stress and E is the Young's modulus. In equation (7), the variable $\gamma^d \geq 0$, which defines the rate of r, represents the damage consistency parameter and, in equation (8), the rate of q is related with the rate of r through the softening modulus H ($H < 0$). Characterization of H is discussed in Section (3).

  - Finally, the classical load-unloading complementarity conditions are given in terms of the expressions (9).

- Elasto-Plastic model ($\sigma_m < 0$): "*ductile*" behaviour:

  - The yield surface, $\psi(\boldsymbol{\sigma}, \xi) = 0$, is defined through equation (10). In that expression, the function $\hat{r}(e(\sigma_m), \theta(\boldsymbol{n}))$, due to Willam and Warnke (1974) (see also Kang and Willam (1999)), defines the roundness of the yield surface when it is intersected by planes parallel to the octahedral one, see Figure 2-(b), and it is given by:

$$\hat{r}(e,\theta) = \frac{4(1-e^2)\cos^2\theta + (2e-1)^2}{2(1-e^2)\cos\theta + (2e-1)\sqrt{4(1-e^2)\cos^2\theta + 5e^2 - 4e}} \tag{19}$$
$$\hat{r}(e,\theta) \in [1, \hat{r}_{max}]$$
$$\hat{r}(e=1,\theta) = 1$$

    Note that $\hat{r}$ depends on the eccentricity function $e(\sigma_m)$ which, in the present work, is defined in terms of the mean stress value as follows:

$$e(\sigma_m) = \hat{e} + [1-\hat{e}]\ exp\,(\omega\,\sigma_m) \quad ; \quad e(\sigma_m = 0) = 1 \quad ; \quad e(\sigma_m \to -\infty) = \hat{e} \tag{20}$$

    where $\hat{e}$ is the eccentricity coefficient. Following to Willam and Warnke (1974), the $\hat{e}$ parameter must satisfy: $\hat{e} \in [0.5; 1]$. In expression (20), ω represents a material parameter which must be

characterized verifying the convexity constraint discussed in Appendix II. Note that the expression (19) jointly with the function (20) defines a circular profile in the octahedral plane ($\sigma_m = 0$) which tends to a triangular profile with large confinement ($\sigma_m \to -\infty$), see Figure 2-(b). Also, $\hat{r}$ depends on the Lode's angle θ, given by:

$$\theta(\boldsymbol{n}) = \frac{1}{3}\arccos\left(\frac{3\sqrt{3}J_3}{2J_2^{\frac{3}{2}}}\right) = \frac{1}{3}\arccos\left(\sqrt{54}\ det(\boldsymbol{n})\right) \tag{21}$$
$$J_3 = \det(\boldsymbol{S})\ ;\ J_2 = \frac{1}{2}(\boldsymbol{S}:\boldsymbol{S})$$

with $\boldsymbol{n}$ as defined in equation (12).

- The β parameter adjusts the limit surface parabolic profile, in the meridian planes, for different levels of confinement, see Section 3 for more details.

- Because $\hat{r} = 1$ whenever $\sigma_m = 0$, the surface given by the plasticity criterion, $\psi(\boldsymbol{\sigma}, \xi) = 0$, intersects the octahedral plane in the circle of radius: $R = \|\boldsymbol{S}\| = (2k_m)^{1/\beta}$, see Figure 2-(b) and 2-(d). Thus, the parameter k_m can be determined by imposing the continuity of the damage and plasticity surfaces, $\hat{g}$ and ψ, through the restriction:

$$\sqrt{2\mu}\ q(r) = (2k_m)^{1/\beta}. \tag{22}$$

The continuity of the surfaces $\hat{g}(\boldsymbol{\sigma}, q) = 0$ and $\psi(\boldsymbol{\sigma}, \xi) = 0$ is forced in the octahedral plane for any value of q, and therefore, for any value of the damage variable d.

- Although it does not appear explicitly in Table 1, we introduce the parameter f_c as the uniaxial compressive ultimate stress. Also it is defined the ratio between the ultimate uniaxial tensile stress (f_t) and the ultimate uniaxial compressive stress (f_c) by means of the expression: $\eta = \frac{f_c}{f_t}$. For concrete, it is: $f_c >> f_t$.

- In the plastic regime, it is postulated the existence of an initial *"yield"* surface, at a rather low level of compressive stresses, $f_c^{'}$ (a fraction of f_c: $f_c^{'} = f_c/\varsigma$), which evolves by means of an adequate hardening-based mechanism here denoted as $\xi(\alpha)$ ($\xi \in [\xi_0, \xi_{max}]$), see equation (11), until reaching a limit surface for $\xi = \xi_{max}$. The successive surfaces, defined by different values of $\xi(\alpha)$, have an identical mathematical expression given by $\psi(\boldsymbol{\sigma}, \xi) = 0$, see Figure 2-(c).

- The plastic flow evolution is non-associative, as the equation (12) shows, and it is governed by the plastic potential function $G(\boldsymbol{\sigma}, \xi)$, which is included in the model, see expression (13). The χ-scalar factor accounts for the allowed degree of dilatancy introduced in the model. Its maximum admissible value is constrained in order to satisfy thermodynamic consistency, see Appendix I for details. Also we define the parameter $\gamma^p \geq 0$ as the plastic multiplier.

- The plastic potential function, $G(\boldsymbol{\sigma}, \xi)$, is also useful for defining the evolution of the scalar internal variable α from its initial null value ($\alpha_0 = 0$), through the relation given by expression (14).

- Equations (15) are the classical plastic load-unloading complementarity conditions.

- From the proposed equations, it can be observed that the evolution of damage decreases the pseudo-cohesion factor k_m, and therefore, it modifies the plastic yield surface $\psi(\boldsymbol{\sigma}, \xi) = 0$. However, damage evolution does not play any role in the evolution equations of the plastic internal variables $\{\boldsymbol{\varepsilon}^p, \alpha\}$. On the other hand, the plastic hardening function only affects the pressure dependent term in the plastic yield function but it does not affect the pseudo-cohesion term. Furthermore, the evolution of plasticity has not any influence in the damage model: neither in their internal variables $\{q, r\}$ nor in the limit surface definition $\hat{g}(\boldsymbol{\sigma}, q) = 0$.

- From the previous observations and the fact that damage and plasticity evolution mechanism are mutually exclusive, it can be concluded that both sub-models are very weakly coupled.

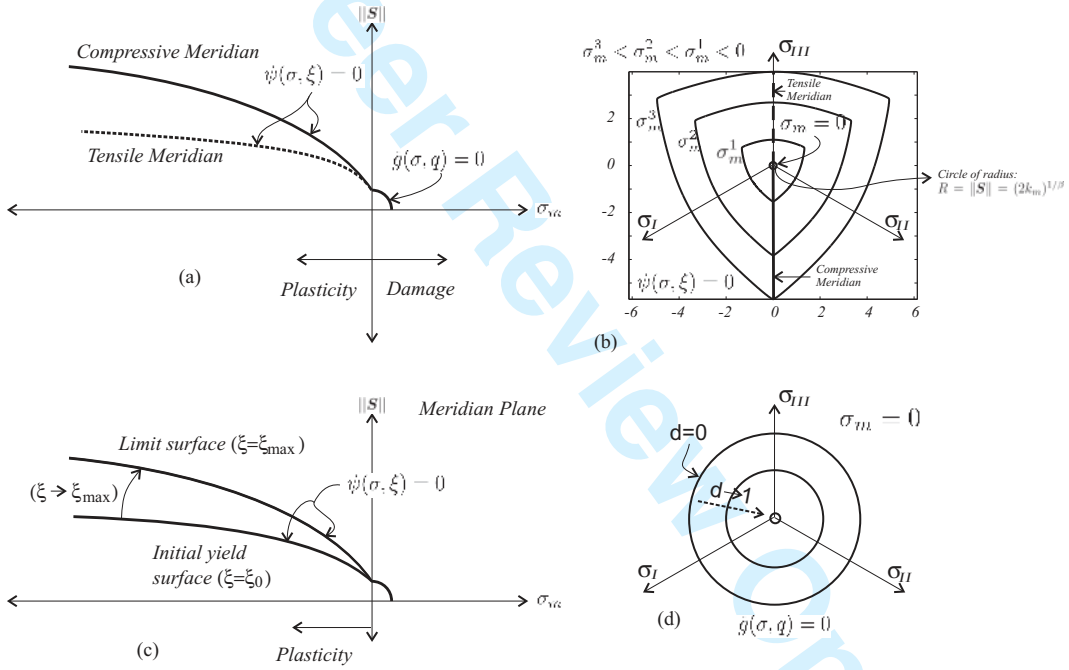

Figure 2: Damage-Plastic model: (a) limit surface representation in the meridian planes $\{\sigma_m, \|\boldsymbol{S}\|\}$; (b) traces of the limit surface with parallel planes to the octahedral one; (c) initial yield and limit surfaces in the plastic regime and their evolution with the parameter $\xi(\alpha)$; (d) evolution, due to damage, of the damage surface intersecting the octahedral plane;

2.1 Constitutive regularization via *CSDA*

In order to preserve the mathematical and physical consistency of the material model, the introduction of strain softening ($H(r) < 0$) due to damage evolution demands some kind of constitutive regularization, such as the

adoption of a material characteristic length. For this reason, the regularization procedure is understood as a fundamental ingredient of the constitutive model.

The so called *Continuum Strong Discontinuity Approach* (*CSDA*) is adopted in the present work as the regularization procedure. The basic foundations and theoretical concepts about the *CSDA* can be found in previous contributions of the authors, see Oliver (2000), Oliver et al. (2002) and Oliver et al. (2005), therefore, this point is here briefly summarized.

As a consequence of material softening, highly strain localization patterns and macro discontinuities (like fractures or cracks) can be developed in the concrete under tensile regimes. This particular phenomenology is considered in the *CSDA* by means of an enhanced kinematical representation which introduces additional *discontinuous* modes in the displacement field. Such kinematics (commonly know as *Strong Discontinuity Kinematics*) can be formally described in terms of the nomenclature displayed in Figure 3.

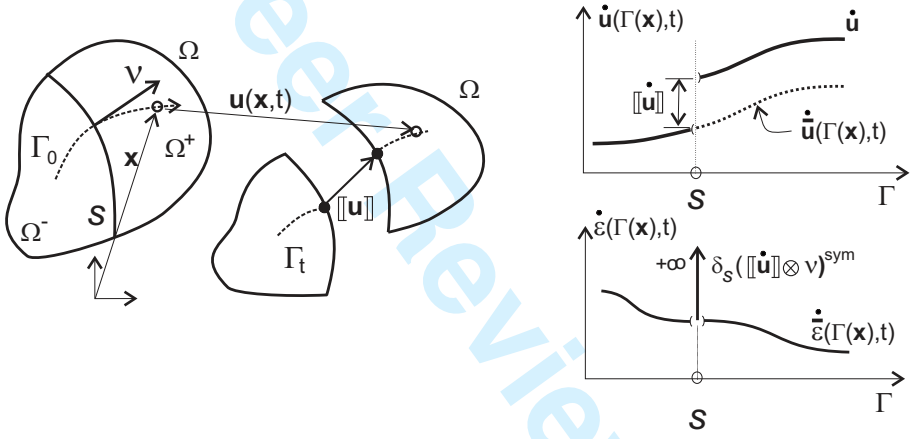

Figure 3: Strong discontinuity kinematics.

Let us consider the reference configuration Ω of a body exhibiting a discontinuity in the displacement field through a material surface $\mathcal{S}$ ($\mathcal{S} \subset \Omega$) with unit normal vector $\boldsymbol{\nu}$. The discontinuity interface $\mathcal{S}$ divides Ω in two sub-domains Ω^+ and Ω^-, with $\boldsymbol{\nu}$ pointing towards Ω^+, see Figure 3. The total displacement field $\boldsymbol{u}(\boldsymbol{x},t)$, compatible with a strong discontinuity kinematics, can be written as the sum of two terms:

$$\boldsymbol{u}(\boldsymbol{x},t) = \overbrace{\overline{\boldsymbol{u}}(\boldsymbol{x},t)}^{\text{continuous}} + \overbrace{\mathcal{H}_{\mathcal{S}}(\boldsymbol{x})\,[\![\boldsymbol{u}]\!](\boldsymbol{x},t)}^{\text{discontinuous}} \quad ; \quad \forall\, \boldsymbol{x} \in \Omega \tag{23}$$

where $\overline{\boldsymbol{u}}(\boldsymbol{x},t)$ and $[\![\boldsymbol{u}]\!](\boldsymbol{x},t)$ are the regular (or smooth) displacement field and the displacement jump, both continuous functions over Ω and $\mathcal{S}$, respectively, and $\mathcal{H}_{\mathcal{S}}(\boldsymbol{x})$ stands for the Heaviside (step) function shifted to the discontinuity interface $\mathcal{S}$, defined as:

$$\mathcal{H}_{\mathcal{S}}(\boldsymbol{x}) = \begin{cases} 0 & \forall \boldsymbol{x} \in \Omega^- \\ 1 & \forall \boldsymbol{x} \in \Omega^+ \end{cases} \quad ; \quad \nabla \mathcal{H}_{\mathcal{S}}(\boldsymbol{x}) = \delta_{\mathcal{S}}(\boldsymbol{x})\,\boldsymbol{\nu} \tag{24}$$

$\delta_{\mathcal{S}}$ being the Dirac's delta-distribution shifted to $\mathcal{S}$. For implementation purposes, we introduce a regularized version of the Dirac's delta function as follow:

$$\delta_{\mathcal{S}} \approx \lim_{k \to \epsilon} \frac{1}{k} \tag{25}$$

with ϵ a very small number, as small as possible.

For geometrically linear problems, the strain tensor compatible with equation (23) can be expressed as:

$$\boldsymbol{\varepsilon}(\boldsymbol{x}, t) = \overbrace{\nabla^s \overline{\boldsymbol{u}} + \mathcal{H}_{\mathcal{S}} \nabla^s [\![\boldsymbol{u}]\!]}^{\overline{\boldsymbol{\varepsilon}}\text{: bounded}} + \overbrace{\delta_{\mathcal{S}} \left(\boldsymbol{\nu} \otimes [\![\boldsymbol{u}]\!]\right)^s}^{\boldsymbol{\varepsilon}^{\delta}\text{: unbounded}} \quad ; \quad \forall\, \boldsymbol{x} \in \Omega \tag{26}$$

where $(\bullet)^s$ represents the symmetry operator for second order tensors. Note that the total strain field has a regular (bounded) and a singular (unbounded) term, denoted as $\overline{\boldsymbol{\varepsilon}}$ and $\boldsymbol{\varepsilon}^{\delta}$, respectively.

The discontinuous kinematical field, $[\![\boldsymbol{u}]\!](\boldsymbol{x})$, represents an independent displacement mode with respect to the standard continuum one $\overline{\boldsymbol{u}}(\boldsymbol{x})$, therefore an additional equation becomes necessary in order to determine the evolution of this term. This additional expression emerges naturally from the traction continuity condition across the interface $\mathcal{S}$:

$$\boldsymbol{t}_{\mathcal{S}} = \boldsymbol{\sigma}_{\mathcal{S}} \cdot \boldsymbol{\nu} = \boldsymbol{\sigma}_{\Omega^+} \cdot \boldsymbol{\nu} \quad ; \quad \forall\, \boldsymbol{x} \in \mathcal{S} \tag{27}$$

where $\boldsymbol{t}_{\mathcal{S}}$ represents the traction vector, $\boldsymbol{\sigma}_{\mathcal{S}}$ is the stress tensor in the discontinuity and $\boldsymbol{\sigma}_{\Omega^+}$ represents the stress state in a point $\boldsymbol{x} \in \Omega^+$ on the boundary $\mathcal{S}$.

A key point in the *CSDA* is that bounded stresses $\boldsymbol{\sigma}_{\mathcal{S}}$ can be evaluated in the interface, even when singular magnitudes of strains ($\boldsymbol{\varepsilon}^{\delta}$) are present, see equation (26). This constitutive regularization is possible due to a redefinition of the continuum strain softening modulus in a distributional sense:

$$H(r) = \delta_{\mathcal{S}}^{-1}\, \overline{H} \quad ; \quad \overline{H} = \delta_{\mathcal{S}}\, H(r) \tag{28}$$

where $\overline{H}$ is the intrinsic softening modulus which can be characterized from the classical specific fracture energy parameter, G_f, used in the *Fracture Mechanics* context of brittle materials, the Young's modulus E and the tensile strength f_t: $\overline{H}(f_t, G_f, E)$. Explicit characterization of $\overline{H}$ is discussed in the next section. The re-interpretation given by expression (28) assures the compatibility between a singular kinematics and the continuum damage material model depicted in Table 1. Besides when the strong discontinuity kinematics, equations (23) and (26), is consistently introduced in this continuum setting, a cohesive-type constitutive law of the form:

$$\boldsymbol{t}_{\mathcal{S}} = \boldsymbol{\sigma}_{\mathcal{S}} \cdot \boldsymbol{\nu} = f([\![\boldsymbol{u}]\!], \text{set of internal variables at } \mathcal{S}) \quad ; \quad \forall\, \boldsymbol{x} \in \mathcal{S} \tag{29}$$

is automatically projected onto the interface $\mathcal{S}$. This traction-separation cohesive model governs the crack evolution in the strong discontinuity regime, see Oliver (2000).

Another important ingredient of the *CSDA* is the criterion to detect the onset and direction of the strong discontinuity mode. In this case, the classical discontinuous material bifurcation condition is used, i.e detection of the localization tensor singularity (see Rudnicki and Rice (1975)). Once detected the material instability condition, the strong discontinuity, with the specific spatial orientation, $\boldsymbol{\nu}$, is embedded into the continuum. The activation of this strong discontinuity changes drastically the isotropic character of the material law, inducing a very marked anisotropic response.

In summary, from the theoretical and computational point of view, the use of the *CSDA* makes possible an efficient treatment of complex degradation mechanisms in the concrete when it is subjected to tensile stress regimes including, for example, the nucleation and propagation of multiple macro-cracks in the medium. The robustness and capabilities of this strategy has been demonstrated in many previous contributions, see Oliver et al. (2005) and Oliver et al. (2006).

3 Material parameter characterization

One of the main features and advantage of the present model is the reduced number of parameters that are necessary to characterize by experimentation in order to completely define it. Most of them can be obtained from simple experimental programs. For conceptual clarity, the set of parameters are classified in different types, as follows:

- Type-1: in this category are included those parameters being strongly dependent of the quality of concrete. Consequently, for each type of concrete, it becomes mandatory to perform the corresponding set of experimental tests in order to identify them.
- Type-2: it includes global definitions about the class of the functions adopted to modelling the softening, $H(r)$, in damage or the hardening mechanism, $\xi(\alpha)$, in the plastic regime (i.e. polynomials functions, exponentials, etc., and their respective coefficients).
- Type-3: it includes the set of parameters that can approximately be calibrated for a wide range of concrete qualities. Once these materials parameters have been adjusted, by using several experimental tests available in the literature, they could be considered as constant parameters in the model, independently of the particular analyzed concrete.

From the previous argument, in Table 2 each one of the material parameters and softening/hardening functions, which have been adopted in the present contribution, are conceptually classified.

Remark: in order to preserve the dimensional consistency of the model, the characterization of parameters performed in this section is independent of the adopted unit system.

	Elasticity		Damage			Plasticity						
Type-1	E	ν	f_t	G_f			f_c					
Type-2					$H(r)$	$\xi(\alpha)$						
Type-3								β	χ	ω	$\hat{e}$	δ	$f_c^{'}$

Table 2: Conceptual classification for different material parameters.

3.1 Type-1 material parameter characterization

The parameters that belong to the previously defined *"Type-1"* are: the elastic Young's modulus E, the Poisson's ratio ν, the ultimate uni-axial tensile stress f_t, the ultimate uniaxial compressive stress f_c and the fracture energy G_f in mode I. All these quantities should be characterized by means of the corresponding laboratory tests.

For notation convenience, in the present contribution the ultimate uni-axial compressive strength f_c is considered to be proportional to the limit uniaxial tensile stress f_t through the relation: $f_c = \eta\, f_t$. The factor "η" depends on the specific concrete type and can take values close to 10, or even higher.

Once defined the Type-1 material parameters, the (undamage or initial) pseudo-cohesion parameter, k_{m0}, can be evaluated as follows:

$$k_{m0} = k_m(q = q_0) = k_{m\,max} = \frac{1}{2}\left[\frac{1}{1+\nu}\right]^{\beta/2} f_t^{\beta} \tag{30}$$

3.2 Type-2 material parameter characterization

Different alternatives for selecting the mathematical expressions of softening/hardening laws, $H(r)$ and $\xi(\alpha)$, for damage and plasticity are possible. Each one of them requires a specific definition and characterization of their corresponding coefficients.

The function that is adopted in the present model for the softening modulus $H(r)$, is given by:

$$H(r) = H_0 \exp\left[H_0\big(\frac{r - r_0}{r_0}\big)\right] \quad ; \quad H_0 = -\frac{f_t^2}{E\,G_f}\, l_{ch} \tag{31}$$

In this equation, the parameter l_{ch}, with dimension of length, is a characteristic size defined as follows: *i)* during the stable material regime it could be adopted as a typical size provided, for example, by the spatial discretization method (finite element mesh size); and *ii)* in the strong discontinuity regime, it is defined as: $l_{ch} = (\delta_S)^{-1} = \epsilon$ (see equation (25)) and, consequently, independent of any kind of spatial discretization method or length scale parameter. From equation (28) and (31), the intrinsic softening modulus results:

$$\bar{H}(r) = \bar{H}_0 \exp\left[H_0\big(\frac{r - r_0}{r_0}\big)\right] \quad ; \quad \bar{H}_0 = -\frac{f_t^2}{E\,G_f} \tag{32}$$

Note that during the strong discontinuity regime, r is of the order $r = \mathcal{O}(1/\epsilon)$, and, from (31) and the definition of l_{ch}, $H_0 = \mathcal{O}(\epsilon)$. Therefore, the exponent term $H_0 r$ is a bounded, not null value. This choice of the softening modulus assures, after the complete material degradation within a band of thickness l_{ch}, a dissipated energy equivalent to the material parameter G_f. In the strong discontinuity regime this thickness tend to zero inducing, on the discontinuity surface, an exponential dependency of the cohesive forces (tractions) with the displacement jumps (crack face separation), see additional details in Oliver (2000).

It is to be noted that the stable material response in tensile stress stages is practically inexistent; then the stable isotropic continuum damage regime, as also the continuum softening modulus (31), plays a subsidiary role in the complete material model description. Thus, the significant parameter for describing the softening law is the intrinsic softening modulus given in expression (32).

The *"limit"* surface in the plastic regime is characterized by assuming, in a uniaxial compressive test, that the surface $\psi(\boldsymbol{\sigma}, \xi) = 0$ is reached at the stress level f_c. And the *"yield"* surface is characterized by assuming, in the same loading path, that the surface $\psi(\boldsymbol{\sigma}, \xi) = 0$ is reached at the stress level $f_c^{'} = f_c/\varsigma$. This is a common assumption in the constitutive modeling of concrete, see for example the contribution of Feenstra and de Borst (1996) and Pivonka et al. (2004). Both criteria give the variation range of ξ which, in the hardening regime, can be assumed as an exponential monotonous increasing function of α, as follows:

$$\xi(\alpha) = \xi_{max} - (\xi_{max} - \xi_0)\exp[-\delta(\alpha/\hat{\sigma}_m^2)] \quad ; \quad \xi(\alpha) \in [\xi_0\,;\,\xi_{max}) \tag{33}$$

The minimum value ξ_0 determines the initial yield surface, and the asymptotic limit value: $\xi_{max} = \lim_{\alpha\to\infty} \xi(\alpha)$ determines the limit surface (Figure 2-(c)). The δ-exponent is an adjustment parameter to be discussed in the next Sub-section. The term $\hat{\sigma}_m$ represents the mean stress value at the moment of yielding. This parameter is computed only once, when the material reaches the inelastic yield surface by the first time, and then it behaves like a constant value. The inclusion of this term plays a key role in the definition of the hardening function $\xi(\alpha)$.

From these ideas, the maximum hardening value (ξ_{max}), can be computed by the following equation:

$$\xi_{max} = \text{cte} = \frac{3}{2}\left[\left(\frac{2}{3}\right)^{\beta/2} - \left(\frac{1}{\eta^2\,(1+\nu)}\right)^{\beta/2}\right] f_c^{\beta-1} \quad ; \quad \eta = \frac{f_c}{f_t} \tag{34}$$

and the minimum hardening value ξ_0, by the equation:

$$\xi_0 = \text{cte} = \frac{3}{2}\left[\left(\frac{2}{3}\right)^{\beta/2} - \left(\frac{1}{\eta^2\,(1+\nu)}\right)^{\beta/2}\right] (f_c^{'})^{\beta-1} \quad ; \quad f_c^{'} = \frac{f_c}{\varsigma} \tag{35}$$

Equations (34) and (35) have been deduced under the hypothesis of undamaged material. Figure 4 displays the influence of a previous, not null, damage value in the profiles of the *"yield"* and *"limit"* surfaces and for the compressive meridian.

It is remarked that assuming equation (33) in the model, is equivalent to adopt a fraction $\Psi^p(\alpha)$ of the internal energy, defined by:

$$\Psi^p(\alpha) = \xi_{max}\,\alpha + (\xi_{max} - \xi_0)\frac{\hat{\sigma}_m^2}{\delta}\exp[-\delta(\alpha/\hat{\sigma}_m^2)] \tag{36}$$

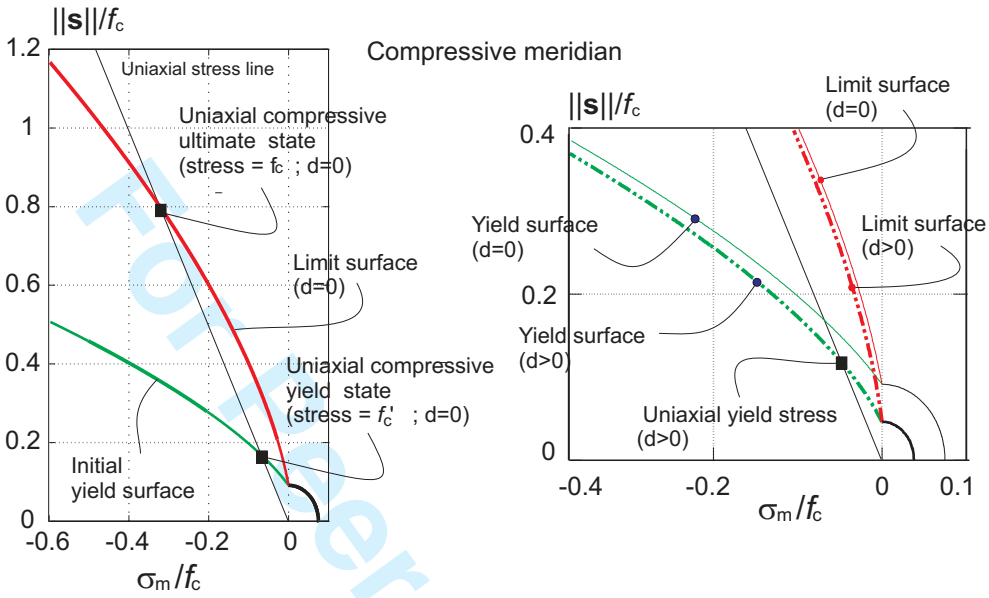

Figure 4: Influence of the damage evolution in the determination of the *"yielding"* and *"limit"* profiles for the plasticity model. Compressive meridian.

The non-associative character of the present constitutive model could induce material instabilities. In spite of this, it has not been detected discontinuous bifurcation in the plastic range. Therefore, it will be accepted that in any compressive stress states the material keeps a stable response.

Remark: Softening in the $\xi(\alpha)$-curve is not included. Consequently the model can not simulate failure (in the sense of complete material stress exhaustion or collapse) in plasticity. The consideration of softening necessarily must be associated to some regularization technique, making useless the adoption of a softening response based exclusively in equivalent stress-strain curves without including specific material characteristic lengths. Unlike the fracture process in tensile stress states, where an objective specific fracture energy describes reasonably well the phenomenology, and therefore a characteristic length is induced by this parameter, the failure modes in confinement states do not seem to be characterized neither by: *i)* a unique magnitude of fracture energy which might be independent of the loading path history, nor by *ii)* a unique characteristic length independent of the stress state. In the authors' opinion, this extremely important topic is an open issue in concrete modeling, and requires a deeper study in order to define an objective softening description in confinement regimes.

3.3 Type-3 material parameter characterization

The following material parameters are grouped in this category: the beta-exponent of the yield and potential plastic functions, the χ-parameter accounting for the dilatant effect, the ω-exponent of the eccentricity func-

tion $e(\sigma_m)$, the constant parameter $\hat{e}$ being the maximum value for the function $e(\sigma_m)$, the δ-exponent of the hardening curve $\xi(\alpha)$ and the uniaxial initial yield stress $f_c^{'}$.

The β-parameter adjusts the limit surface profile in the meridian planes $\{\sigma_m, \|\boldsymbol{S}\|\}$. By using several concrete experimental test for different confinement stress regimes, such as those presented in Kang and Willam (1999) and reproduced in Figure 5, it is possible to obtain a good fitting for β and is given by: $\beta = 1.6$.

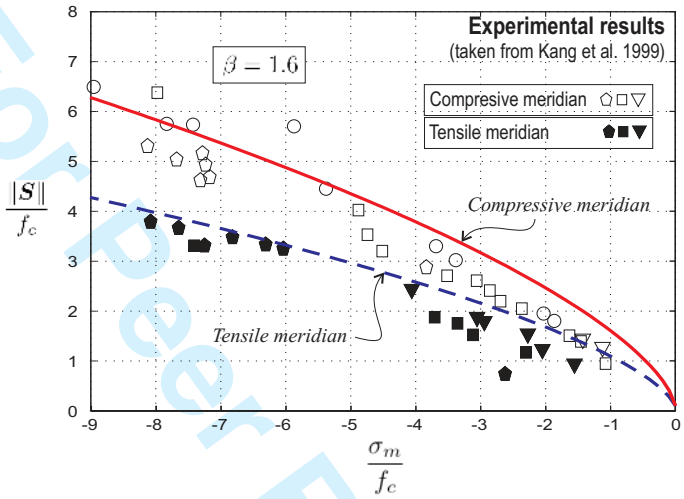

Figure 5: Characterization of β-exponent from available experimental data.

Appendix I presents a thermodynamic admissibility condition by which, an upper bound χ^*_{max} for the dilatant χ-parameter is obtained. Besides, Appendix II determines, via a yield surface convexity argument, the upper admissible bound ω^*_{max} for the ω-coefficient. Considering these constraints, the set of Type-3 parameters have been adjusted through several experimental tests, showed in Section (5), and resulting:

$$\chi = 0.005 \leq \chi^*_{max} \quad \text{(thermodynamic admissibility condition)} \tag{37}$$

$$\omega = 0.41\ \frac{\xi_0}{k_{m\,0}} \leq \omega^*_{max} \quad \text{(convexity yield surface condition)} \tag{38}$$

$$\hat{e} = 0.54 \tag{39}$$

$$\delta = 6000\ \eta^2\ f_t^{\beta} \tag{40}$$

$$\varsigma = \eta \qquad ; \qquad (f_c^{'} = f_t) \tag{41}$$

4 Numerical integration algorithm

The numerical integration scheme of the damage-plastic model can be performed using a very simple, efficient and robust algorithm. It is based on the Impl-Ex method, described in Oliver et al. (2008), and uses a double evaluation of stresses per time step: *i)* one stress value is obtained through a standard implicit (Backward-Euler)

return mapping scheme; *ii)* the second one is determined via an explicit extrapolation of implicit values obtained in previous time steps.

The equilibrium condition is then calculated with the explicit stresses. Therefore, the algorithmic tangent tensor, used in the iterative global equilibrium condition, is the derivative of the explicit stresses respect to the incremental strains. With minimum additional assumptions on the stress extrapolation scheme, this tensor is positive definite in all the cases.

In the following two subsections, we describe both integration schemes: the implicit and Impl-Ex stress evaluations.

4.1 Implicit integration scheme

Given the strains $\boldsymbol{\varepsilon}_{t+\Delta t}$ at step $t+\Delta t$, Box 1 describes the implicit integration scheme to evaluate the stress $\boldsymbol{\sigma}_{t+\Delta t}$. Holding fixed the internal variables of the model, a trial stress value, $\boldsymbol{\sigma}^{trial}$, is first calculated with the incremental strains. The mean value of $\boldsymbol{\sigma}^{trial}$ defines if damage or plastic process is active in the step.

a) Damage model implicit integration

The first case could happen when the mean trial stress value is greater or equal to zero. Then, plastic variables, $\boldsymbol{\varepsilon}^p, \alpha, \xi$, stay fixed in the step . Decision if damage evolution happens, is based on the trial value of the internal variable r and its comparison with the value in the previous step. The implicit integration is then performed in closed form, see Box 2, as it was explained in previous papers of the authors (see Oliver et al. (2002)).

b) Plastic model implicit integration

Alternatively, with negative mean trial stress value, the damage variables, r and q, remain constant and plastic evolution is active when $\psi^{trial} = \psi(\boldsymbol{\sigma}^{trial}, \xi_t)$ is greater or equal to zero, see Box 3. If $\psi^{trial} \geq 0$, a Backward-Euler scheme is applied to the plastic model equations, defining the following updates of stresses and internal variables:

$$\boldsymbol{\sigma}_{t+\Delta t} = \boldsymbol{\sigma}^{trial} - \gamma^p \left(\frac{q_{t+\Delta t}}{r_{t+\Delta t}} \mathbb{C}^e \right) : \left(\frac{\beta}{2} \parallel \boldsymbol{S}_{t+\Delta t} \parallel^{\beta-1} \boldsymbol{n} + \chi \xi_{t+\Delta t} \mathbb{1} \right) \tag{42}$$

$$\alpha_{t+\Delta t} = \alpha_t - \gamma^p \chi \sigma_{m_{t+\Delta t}} \tag{43}$$

$$\xi_{t+\Delta t} = \xi(\alpha_{t+\Delta t}) \tag{44}$$

jointly with the plastic consistency:

$$\psi_{t+\Delta t} = \frac{\hat{r}(e(\sigma_{m_{t+\Delta t}}), \theta(\boldsymbol{n}_{t+\Delta t}))}{2} \parallel \boldsymbol{S}_{t+\Delta t} \parallel^{\beta} + \xi_{t+\Delta t} \sigma_{m_{t+\Delta t}} - k_m = 0 \tag{45}$$

BOX 1: Implicit backward-Euler integration scheme for the damage-plastic concrete model (step: $t + \Delta t$).

DATA : *given* $\boldsymbol{\varepsilon}_{t+\Delta t}, r_t, q_t, \boldsymbol{\varepsilon}^p_t, \alpha_t, \xi_t$; ***FIND :*** $r_{t+\Delta t}, q_{t+\Delta t}, \boldsymbol{\sigma}_{t+\Delta t}, \boldsymbol{\varepsilon}^p_{t+\Delta t}, \alpha_{t+\Delta t}, \xi_{t+\Delta t}$

Compute the trial stress value: $\boldsymbol{\sigma}^{trial} = \frac{q_t}{r_t}\mathbb{C}^e : (\boldsymbol{\varepsilon}_{t+\Delta t} - \boldsymbol{\varepsilon}^p_t)$

IF $(tr(\boldsymbol{\sigma}^{trial}) \geq 0)$ ***THEN***

$\boldsymbol{\varepsilon}^p_{t+\Delta t} = \boldsymbol{\varepsilon}^p_t$; $\alpha_{t+\Delta t} = \alpha_t$; $\xi_{t+\Delta t} = \xi_t$

Implicit damage model, see BOX 2

ELSEIF $(\text{tr}(\boldsymbol{\sigma}^{trial}) < 0)$ **THEN**

$r_{t+\Delta t} = r_t$, $q_{t+\Delta t} = q_t$

Implicit plastic model, see BOX 3

ENDIF

Equation (42) can be decomposed into the hydrostatic component:

$$\sigma_{m_{t+\Delta t}} = \sigma^{trial}_m - \gamma^p \kappa_q \chi \xi_{t+\Delta t} \tag{46}$$

where $\kappa_q = \frac{q_{t+\Delta t}}{r_{t+\Delta t}} \frac{E}{3(1-2\nu)}$; and the deviatoric component. After considering that the tensor $\boldsymbol{n}_{t+\Delta t}$, representing the direction of the deviatoric stress $\boldsymbol{S}_{t+\Delta t}$, is identical to that of $\boldsymbol{n}^{trial}$, the deviatoric tensorial equation derived from (42) can be rewritten in terms of a scalar equation, as follows:

$$\| \boldsymbol{S}_{t+\Delta t} \|^{\beta} = \| \boldsymbol{S}^{trial} \|^{\beta} - \gamma^p \mu_q \beta \| \boldsymbol{S}_{t+\Delta t} \|^{\beta-1} \tag{47}$$

where $\mu_q = \frac{q_{t+\Delta t}}{r_{t+\Delta t}} \frac{E}{2(1+\nu)}$.

Therefore, the equation system that must be solved, in order to find the updated variables, are (43)–(47). Box 3 proposes a scheme to solve this equation system. An internal loop solves via an iterative Newton-Raphson scheme, and fixing α, ξ and $\hat{r}$, the equations (45), (46) and (47) in order to find $\| \boldsymbol{S}^j_{t+\Delta t} \|$, $\sigma^j_{m_{t+\Delta t}}$ and γ^p. In an external loop, the variables α and ξ, jointly with $\hat{r}$, are updated. The procedure follows until reaching the convergence of the complete equation system (43)–(47).

BOX 2: Implicit backward-Euler integration scheme for the damage model (step: $t + \Delta t$).

DATA : *given* $\boldsymbol{\varepsilon}_{t+\Delta t}, r_t, q_t, \boldsymbol{\sigma}^{trial}$; ***FIND :*** $r_{t+\Delta t}, q_{t+\Delta t}, \boldsymbol{\sigma}_{t+\Delta t},$

Compute damage loading-unloading condition: $r^{trial} = \sqrt{\boldsymbol{\sigma}^{trial} : \boldsymbol{\varepsilon}_{t+\Delta t}}$

IF $(r^{trial} > r_t)$ ***THEN***

Damage evolution:

$r_{t+\Delta t} = r^{trial}$; $q_{t+\Delta t} = q_t + H[r_{t+\Delta t} - r_t]$; $\boldsymbol{\sigma}_{t+\Delta t} = \frac{q_{t+\Delta t}}{r_{t+\Delta t}} \mathbb{C}^e : (\boldsymbol{\varepsilon}_{t+\Delta t} - \boldsymbol{\varepsilon}_t^p)$

ELSE

Elastic unloading:

$r_{t+\Delta t} = r_t$; $q_{t+\Delta t} = q_t$; $\boldsymbol{\sigma}_{t+\Delta t} = \boldsymbol{\sigma}^{trial}$

ENDIF

We observe that, equation (47) corresponds to a radial return mapping in the octahedral plane. The Lode's angle θ, of the updated stresses, verifies that: $\theta(\boldsymbol{n}_{t+\Delta t}) = \theta(\boldsymbol{n}^{trial})$. This property is exploited in Box 3.

BOX 3: Implicit backward-Euler integration scheme for the plastic concrete model (step: $t + \Delta t$).

DATA : *given* $\boldsymbol{\sigma}^{trial} = \boldsymbol{S}^{trial} + \sigma_m^{trial}\mathbb{1},\ \boldsymbol{\varepsilon}_n^p,\ \alpha_n$

FIND : $\boldsymbol{\sigma}_{t+\Delta t},\ \boldsymbol{\varepsilon}_{t+\Delta t}^p,\ \alpha_{t+\Delta t},\ \gamma^p$

Evaluate: $\psi^{trial} = \frac{\hat{r}_t}{2} \parallel \boldsymbol{S}^{trial} \parallel^{\beta} - \xi(\alpha_t)\sigma_m^{trial} - k_m$

IF $(\psi^{trial} > 0)$ **THEN**

Plastic evolution: return mapping scheme:

EXTERNAL LOOP: j ***WHILE*** $(R2 >$ ***tol*** $\&\ R3 >$ ***tol***$)$

Using a Newton-Raphson procedure, solve the equation system:

$R1 = 0; R2 = 0; R3 = 0$

INTERNAL LOOP : i *(Newton-Raphson:* $\xi_{t+\Delta t}^{j-1}$ *and* $\hat{r}_{t+\Delta t}^{j-1}$ *remain fixed in the loop)*

$$R1 = \parallel \boldsymbol{S}_{t+\Delta t} \parallel^{\beta} + \gamma^p \mu_q \beta \parallel \boldsymbol{S}_{t+\Delta t} \parallel^{\beta-1} - \parallel \boldsymbol{S}^{trial} \parallel^{\beta} = 0$$

$$R2 = \sigma_{m_{t+\Delta t}} + \gamma^p \chi \kappa_q \xi - \sigma_m^{trial} = 0$$

$$R3 = \frac{\hat{r}}{2} \parallel \boldsymbol{S}_{t+\Delta t} \parallel^{\beta} + \xi \sigma_{m_{t+\Delta t}} - k_m = 0$$

END INTERNAL LOOP : i (End Newton-Raphson iteration)

Newton-Raphson solution : $\parallel \boldsymbol{S}_{t+\Delta t} \parallel_{t+\Delta t}^{j}\ ;\ \sigma_{m_{t+\Delta t}}^{j}\ ;\ (\gamma^p)^j$

Update:

$$\alpha_{t+\Delta t}^{j} = \alpha_t - (\gamma^p)^j \chi \sigma_{m_{t+\Delta t}}^{j}$$

$$\xi_{t+\Delta t}^{j} = \xi_{max} - (\xi_{max} - \xi_0)\exp\left(-\delta \frac{\alpha_{t+\Delta t}^{j}}{\hat{\sigma}_m^2}\right)$$

$$\hat{r} = \hat{r}(e(\sigma_{m_{t+\Delta t}}^{j}), \theta(\boldsymbol{n}^{trial}))$$

Evaluate:

$$R2 = \hat{R2}(\xi_{t+\Delta t}^{j}, \sigma_{m_{t+\Delta t}}^{j}, (\gamma^p)^j)$$

$$R3 = \hat{R3}(\xi_{t+\Delta t}^{j}, \sigma_{m_{t+\Delta t}}^{j}, \boldsymbol{S}_{t+\Delta t}^{j})$$

END EXTERNAL LOOP: j

$$\boldsymbol{\sigma}_{t+\Delta t} = \boldsymbol{S}_{t+\Delta t} + \sigma_{m_{t+\Delta t}}\mathbb{1}$$

$$\boldsymbol{\varepsilon}_{t+\Delta t}^p = \boldsymbol{\varepsilon}_t^p + \gamma^p \left(\frac{\beta}{2} \frac{\boldsymbol{S}_{t+\Delta t}^{\beta}}{\|\boldsymbol{S}_{t+\Delta t}\|} + \chi \frac{\xi(\alpha_{t+\Delta t})}{3}\mathbb{1} \right)$$

ELSE

Elastic unloading:

$$\boldsymbol{\sigma}_{t+\Delta t} = \boldsymbol{\sigma}^{trial}$$

$$\boldsymbol{\varepsilon}_{t+\Delta t}^p = \boldsymbol{\varepsilon}_t^p$$

$$\alpha_{t+\Delta t} = \alpha_t$$

ENDIF

4.2 Stress explicit integration procedure

Box 4 proposes an explicit extrapolation scheme for the stresses and the corresponding algorithmic tangent tensor. With the condition that $\beta < 2$, it is easily shown that the three coefficients of the tensor $\mathbb{C}_{alg}$ are positive which assure its positive definite character.

BOX 4: Explicit integration scheme for the damage-plastic concrete model (step: $t + \Delta t$).

DATA : *given* $\boldsymbol{\varepsilon}_{t+\Delta t}$ *and (from BOX 1)* the implicit values from previous steps:

$$r_t, r_{t-\Delta t}, q_t, \parallel \boldsymbol{S}_t \parallel, \sigma_{m_t}, \boldsymbol{\varepsilon}_t^p, \alpha_t, \gamma_t^p$$

Compute explicit extrapolation:

$$\tilde{\gamma}^d = \frac{\Delta t_{t+\Delta t}}{\Delta t_t}(r_t - r_{t-\Delta t}) \qquad \text{and} \qquad \tilde{\gamma}^p = \frac{\Delta t_{t+\Delta t}}{\Delta t_t}\gamma_t^p$$

Update internal and damage variables:

$$\tilde{r} = r_t + \tilde{\gamma}^d \qquad \text{and} \qquad \tilde{\alpha} = \alpha_t - \tilde{\gamma}^p \chi \sigma_{m_t}$$

$$\tilde{q} = q_t + H\tilde{\gamma}^d \qquad \text{and} \qquad \tilde{\xi} = \xi(\tilde{\alpha})$$

$$\kappa_{\tilde{q}} = \frac{\tilde{q}}{\tilde{r}} \frac{E}{3(1-2\nu)} \qquad ; \qquad \mu_{\tilde{q}} = \frac{\tilde{q}}{\tilde{r}} \frac{E}{2(1+\nu)}$$

Compute explicit trial stress values:

$$\tilde{\boldsymbol{\sigma}}^{trial} = \frac{\tilde{q}}{\tilde{r}} \mathbb{C}^e : (\boldsymbol{\varepsilon}_{t+\Delta t} - \boldsymbol{\varepsilon}_t^p)$$

Compute explicit stresses:

$$\tilde{\boldsymbol{\sigma}}_{t+\Delta t} = \tilde{\boldsymbol{S}} + \tilde{\sigma}_m \mathbb{1}$$

$$\tilde{\sigma}_m = \tilde{\sigma}_m^{trial} - \kappa_{\tilde{q}} \tilde{\gamma}^p \chi \tilde{\xi}$$

$$\tilde{\boldsymbol{S}} = \parallel \tilde{\boldsymbol{S}} \parallel \boldsymbol{n}^{trial}; \qquad \parallel \tilde{\boldsymbol{S}} \parallel = \parallel \boldsymbol{S}_t \parallel + \Delta \parallel \tilde{\boldsymbol{S}} \parallel$$

$$\Delta \parallel \tilde{\boldsymbol{S}} \parallel = \frac{1}{Den_1} \left[\parallel \tilde{\boldsymbol{S}}^{trial} \parallel - (\parallel \boldsymbol{S}_t \parallel + \beta \mu_{\tilde{q}} \tilde{\gamma}^p \parallel \boldsymbol{S}_t \parallel^{\beta-1}) \right]$$

$$Den_1 = 1 + \beta(\beta - 1)\mu_{\tilde{q}} \tilde{\gamma}^p \parallel \boldsymbol{S}_t \parallel^{\beta-2}$$

Compute the Impl-Ex algorithmic tangent operator:

$$\tilde{\mathbb{C}}_{alg} = \kappa_{\tilde{q}}(\mathbb{1} \otimes \mathbb{1}) + 2\mu_{\tilde{q}} \frac{\|\tilde{\boldsymbol{S}}\|}{\|\tilde{\boldsymbol{S}}^{trial}\|} \mathbb{I}^{dev} + 2\mu_{\tilde{q}} \left(\frac{1}{Den_1} - \frac{\|\tilde{\boldsymbol{S}}\|}{\|\tilde{\boldsymbol{S}}^{trial}\|} \right) (\boldsymbol{n}^{trial} \otimes \boldsymbol{n}^{trial})$$

$$\mathbb{I}^{dev} = \mathbb{I} - \frac{1}{3}(\mathbb{1} \otimes \mathbb{1})$$

Remark: the robustness of the proposed integration algorithm is given by three facts:

(i) the intersection between the damage criterion surface and the plastic yield function is a circle which remains in the octahedral plane, even during material degradation processes;

(ii) the decision about if the material responds with damage or plasticity can be established a-priori, in terms of the trial stress, not changing in the course of the return mapping iterations. The independent integration of every sub-model is, therefore, easily performed,

(iii) Due to the positive definite character of the algorithmic tangent tensor, the *Impl-Ex* scheme provides an additional numerical stability feature, particularly in the material softening regime.

In summary, the numerical integration scheme for the constitutive model that we propose in this section is a direct extension of a previous method of the authors. In that contribution they have addressed issues related with: robustness, convergence and numerical stability conditions of the integration scheme. Also, it is shown the advantages of its application to problems involving material failure. The conclusions published in that work are trivially extended to the present application. Thus, the interested lector could obtain additional information in the referenced paper.

5 Validation of the model using experimental tests

The following experimental tests performed on concrete specimens, were presented in the paper of Cervenka and Papanikolaou (2008) and have been taken from previous experimental classical works. Here, they are reproduced in order to characterize the parameters, particularly those corresponding to Type-3, and validate the present concrete model.

Type-1 material parameters for simulating the different concrete qualities in the tests, are taken from Cervenka et al. and displayed in Table 3. The remaining set of parameters have been adjusted in order to fit the experimental tests in this Section and their values are defined by expressions (37–41).

$f_c[MPa]$	20	30	40	50	60	70	80	90	100	110
$E[MPa]$	24377	27530	30011	32089	33893	35497	36948	38277	39506	40652
ν	0.2	0.2	0.2	0.2	0.2	0.2	0.2	0.2	0.2	0.2
$\eta = \frac{f_c}{f_t}$	10.15	12.26	13.76	15.04	16.18	17.24	18.16	19.03	19.85	20.63

Table 3: Material parameters for different concrete qualities. Uni-Bi and Triaxial tests.

In the Figures 6, 7, 8, 9 and 10, experimental values are displayed with symbols. The model responses correspond to the plain curves, without symbols.

Remark: in compressive loading tests, and as it was mentioned, the present model predicts results only during the material hardening regime. Therefore, in this section, all the numerical validations are shown up to reaching the limit load values of the experimental results.

5.1 Uni-axial, Bi-axial and Tri-axial tests

A set of uni-axial compression tests (without confinement) carried out in specimens of different concrete qualities, described in terms of their ultimate compressive strength f_c, are displayed in Figure 6. The concrete strength ranges from $f_c = 21.7\,[MPa]$ to $f_c = 105.7\,[MPa]$.

These tests display the fitting of the model response during the non-linear hardening regime captured by the function $\xi(\alpha)$, as also, the comparative strains at the peak load values. Obviously that, due to the selection method

of the material model parameters above described, the experimental limit values f_c are reproduced exactly by the model in all these cases.

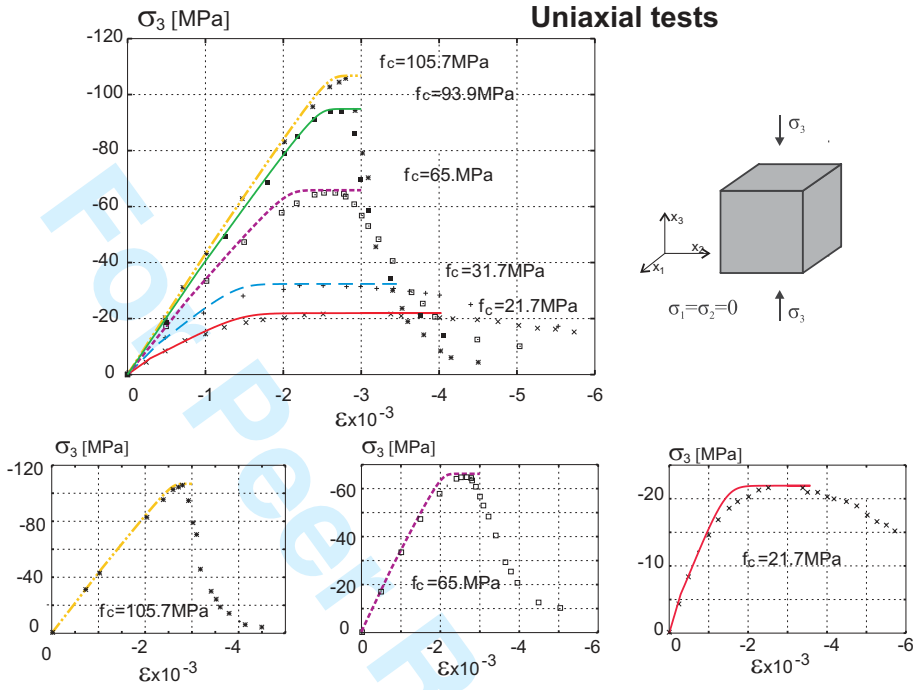

Figure 6: Strain-Stress curves in uni-axial tests for different concrete qualities. Experimental values from Dahl (1992) (taken from Cervenka et al.) are displayed in symbols. Bottom plots correspond to a single pair of curves in the upper plots.

Bi-axial ($\sigma_2 = 0.52\sigma_3$), equi-biaxial ($\sigma_2 = \sigma_3$) and one uni-axial $\sigma_1 = \sigma_2 = 0$ tests are displayed in Figure 7 and Figure 8. In all these cases the maximum limit load has been adequately captured by the model, as also, the material non-linear responses until to reach the peak load value. It is remarked that the σ_3-ε_2 response of the biaxial test ($\sigma_2 = 0.52\sigma_3$), in Figure 7, has been particularly useful for calibrating the χ-dilatant parameter of the model.

Tri-axial compression tests, subjected to different confinement levels, are displayed in Figures 9 and 10 for different concrete qualities. The numerical solutions have been obtained imposing the following loading path: first one hydrostatic pressure is applied, and after that, an increase of only one principal stress (σ_3) is defined.

5.2 Plane stress condition

Figure 11 presents, in the principal stress space, the concrete failure values corresponding to the widely known biaxial experimental results of Kupfer and Gerstle (1973). In the Figure, it is also plotted the present model limit prediction curve determined with an identical set of parameters to those characterized in the previous subsection, and they are displayed in the Figure.

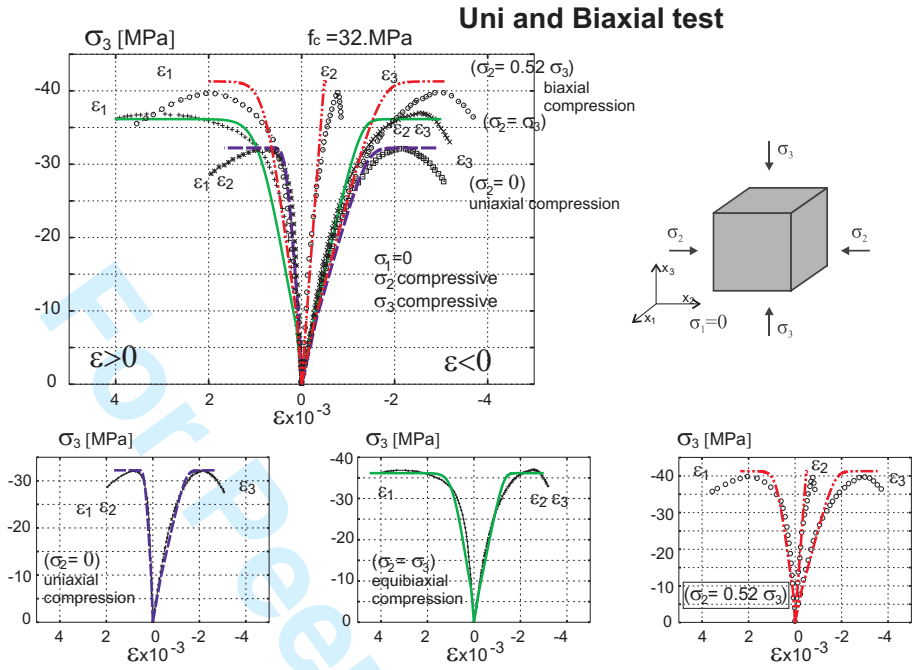

Figure 7: Strain-Stress curves in bi-axial tests (concrete strength: $f_c = 32\,[MPa]$). Experimental values from Kupfer et al. (1969) (taken from Cervenka et al.) are displayed in symbols. Bottom plots correspond to a single pair of curves in the upper plots.

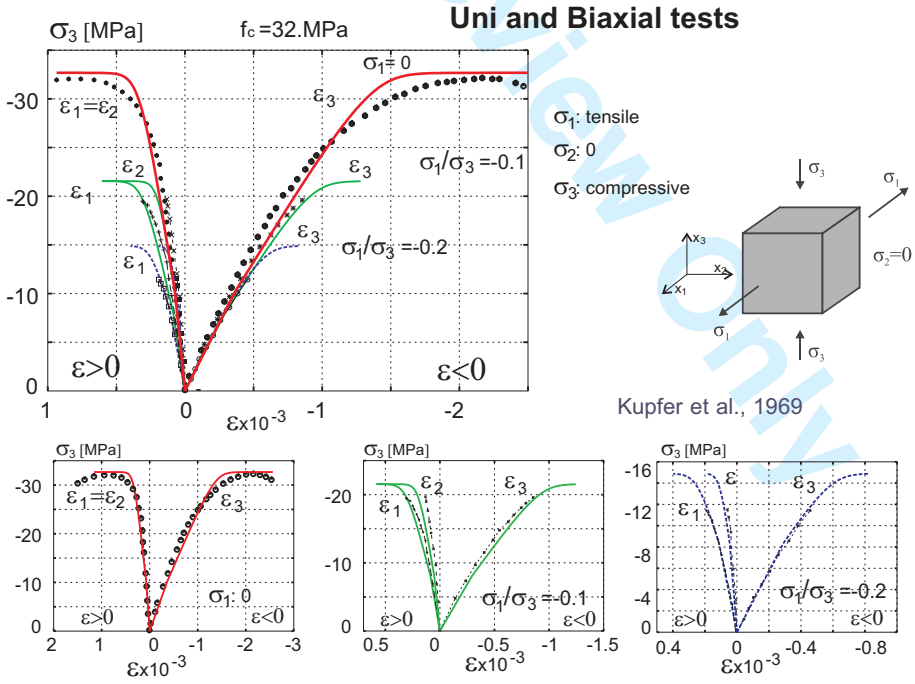

Figure 8: Strain-Stress curves in bi-axial tests (concrete strength: $f_c = 32\,[MPa]$). Experimental values from Kupfer et al. (1969) (taken from Cervenka et al.) are displayed in symbols. Bottom plots correspond to a single pair of curves in the upper plots.

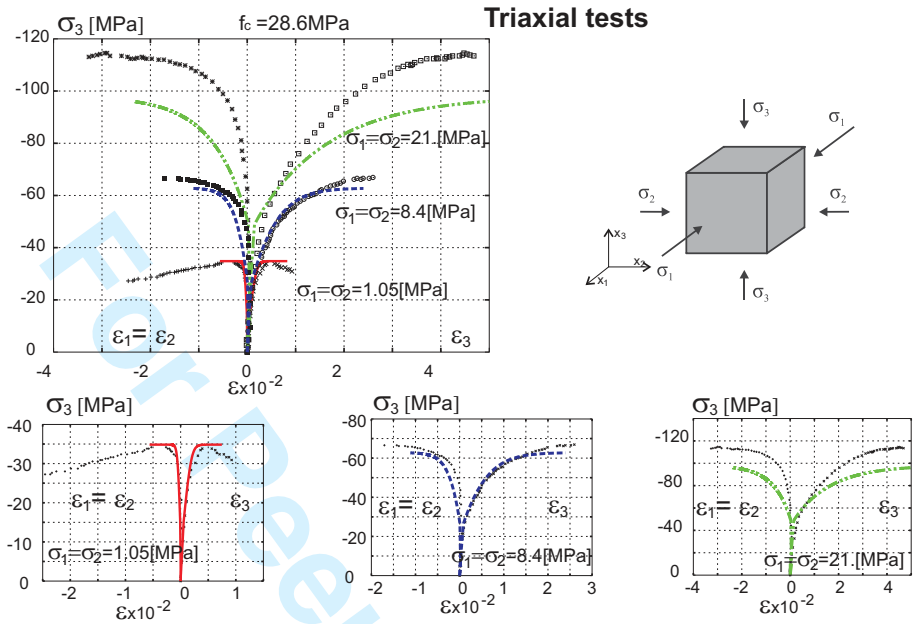

Figure 9: Strain-Stress curves in tri-axial tests (concrete strength: $f_c = 28.6\,[MPa]$) and different levels of confinements. Numerical solution vs. experimental solutions from Imran (1994) (taken from Cervenka et al.). Bottom plots correspond to a single pair of curves in the upper plots.

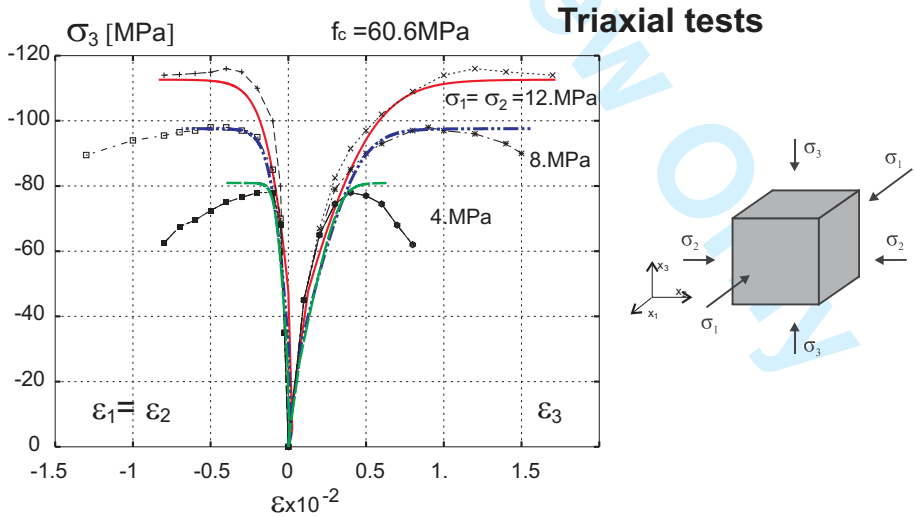

Figure 10: Strain-Stress curves in tri-axial tests (concrete strength: $f_c = 60.6\,[MPa]$) and different levels of confinements. Numerical solution vs. experimental solutions from Candappa et al. (2001) (taken from Cervenka et al.)

It is particularly remarked in these tests the results corresponding to the second and fourth quadrant of the Figure 11. In fact, in those stress regimes, the experimental results display a trend to decrease the concrete limit tensile stress when high compressive stresses are applied in the transversal direction. The present model predicts a correct trend in those cases.

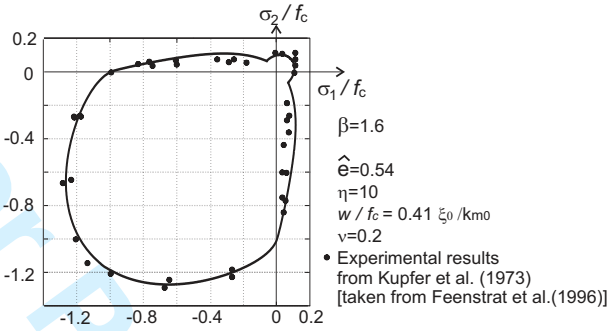

Figure 11: Comparison of the model limit strength prediction, in plane stress conditions, with experimental data of Kupfer and Gerstle (1973).

6 A classical concrete beam test

On the early 1960's, Bressler and Scordelis performed a series of 12 rectangular cross section reinforced concrete beam tests which were recently closely reproduced by Vecchio and Shim (2004). These tests have been adopted as benchmarks for validating several Finite Element codes.

From the last reference, the beam case A3 has been taken in order to validate and evaluate the present numerical model. This case consists of a three-point beam with dimensions displayed in Figure 12-(b). The cross-section details, dimensions and amount of longitudinal and shear (closed stirrups) reinforcements, are given in Figure 12-(a).

The A3 beam case is characterized by a heavy longitudinal bottom reinforcement which, jointly with the shear reinforcements, generates a flexure-compression failure mode being mainly governed by the crushing of the concrete. Therefore, in this case, a correct capturing of the structural limit load estimation is mostly based on a good estimation of the concrete model response in compressive stress states.

6.1 Materials

The Type-1 material parameters of the model are given in Table 4 and have been taken from Vecchio and Shim (2004). Symbols denotes: A_S: bar areas, σ_Y: steel yield stress, E and E_S: Young's modulus, f_c: ultimate compressive stress, f_t: ultimate tensile stress, G_f: fracture energy. In particular, it is mentioned that: *i)* the steel bar reinforcements are modeled through a 1D perfectly plastic response without considering any hardening/softening

law; *ii)* the concrete fracture energy G_f was not reported in the reference work, therefore, it has been adopted a standard value for concrete, as also, the Poisson's ratio which is taken: $\nu = 0.2$.

Type 2 and 3 material parameters are identical to those characterized in Section 3.

Reinforcement steel			
Bar type	$A_s\, mm^2$	$\sigma_Y\, [MPa]$	$E_S\, [GPa]$
M10	100.	315	200.
M25	500.	440	210.
M30	700.	436	200.
D4	25.7	600	200.
Concrete			
$f_c\, [MPa]$	$f_t\, [MPa]$	$G_f\, [N/m]$	$E\, [GPa]$
43.5	2.47	100.	34.3

Table 4: Three-point beam. Description of the material parameters, taken from Vecchio and Shim (2004): beam case A3.

6.2 Numerical model: mixture theory for the composite and FE mesh

The numerical simulation is obtained with a 2D plane strain model. Even when this assumption is a crude approach for reproducing the triaxial stress state, the model provides a good description of some important phenomenological issues. And, more importantly, for reaching the objectives we pursue in this work, because it reproduces closely the concrete crushing phenomenon and its effects on the failure mode.

The finite element mesh, displayed in Figure 12-(b), discriminates two different zones. The plain concrete zone, where the material is modeled using the constitutive relation presented in previous sections, and those corresponding to the reinforcements and its neighborhood. In the last zones, the material is simulated through the mixture theory presented in Linero (2006), where a fraction of the volumetric material is considered concrete and the remaining part is steel. The concrete in this region is approached with the same constitutive model as the plain concrete, while the steel responds with a perfect elasto-plastic law in the reinforcement direction. In the present simulation, it is assumed a perfect concrete-steel adherence, without slipping between both components. A more detailed numerical model could be used for simulating RC elements, including a meso-structural description of the material constituents (concrete, reinforcements and interfaces), see for example Sánchez et al. (2010).

Figure 12-(c) displays the load P vs the vertical displacement (Δu_A) of the load application point. In the plot, we compare the numerical solution with the experimental curve taken from Vecchio et. al. Also , it is included a numerical solution provided by the reference work. The maximum load of the present numerical solution is: $P^{ult} = 425kN$, at a vertical displacement $\Delta u_A^{ult} = 42mm$, which must be contrasted with the experimental values (Table 6 in the reference work of Vecchio and Shim (2004)): $P^{ult} = 420kN$, and $\Delta u_A^{ult} = 51mm$, respectively. Whereas, the similar Bresler-Scordelis test provided the following results: $P^{ult} = 467kN$, and $\Delta u_A^{ult} = 35.3mm$.

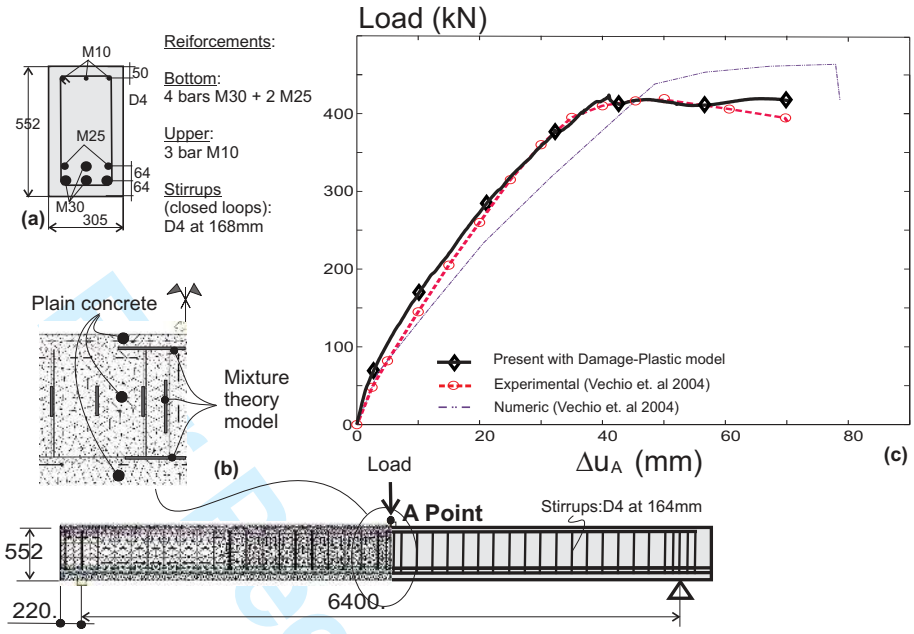

Figure 12: A concrete beam test: (a) cross section details; (b) reinforced concrete beam model, finite element mesh and assumed material models in different regions of the beam; (c) plot of the load versus mid-span vertical displacement, experimental and numerical results. (Dimensions in [mm]).

Figure 13 displays additional results. From the reference work, it is reproduced in Figure 13-(a), the crack pattern observed in the experimental test, as also the concrete crushing below the load application point. Figures 13-(c:d) display the distribution of: damage, x-isodisplacement curves and α variables, respectively, in the end of the analysis ($\Delta u_A = 89.mm$). The damage field represents a rather distributed crack pattern, which reproduces the experimental observation. However, the x-isodisplacement curves depict only one active crack (in the midspan) which is opening at the end of analysis. The remaining cracks have not been completely developed. Figure 13-(e) displays the damage distribution at a loading stage corresponding with $\Delta u = 5.8mm$, which is approximately the 15% of Δu_A^{ult} and corresponds to the beginning of the fracturing process, such as reported in the experimental observation.

6.3 Discussion of results

The failure mode for the A3 beam reported in Vechio et al., as also in the similar Bressler et al. test, corresponds to "concrete crushing in the compression zone without a notable splitting in the tensile zone. Cracks in tensile, formed at loads of approximately 15% of ultimate load and propagated as loading increased; however, major diagonal-tension cracks did not develop. Failure was sudden and brittle" (textually taken from Vecchio and Shim (2004)).

From the experimental evidence, our results capture reasonably well the following phenomenology of the test: i) the crushing of concrete in the midspan; ii) the tensile fracture pattern and its evolution during the loading

process and iii) the ultimate structural load. Additionally, it is remarked that a correct capturing of the structural limit load estimation is mostly based on a good prediction of the concrete model response in compressive stress states.

The sudden failure at $\Delta u_A \approx 71mm$ was not captured by the present model. The authors consider that it is manly due to that softening mechanism has not been taken into account in the concrete model plastic regime, as also, to the perfect plastic response of the steel reinforcements.

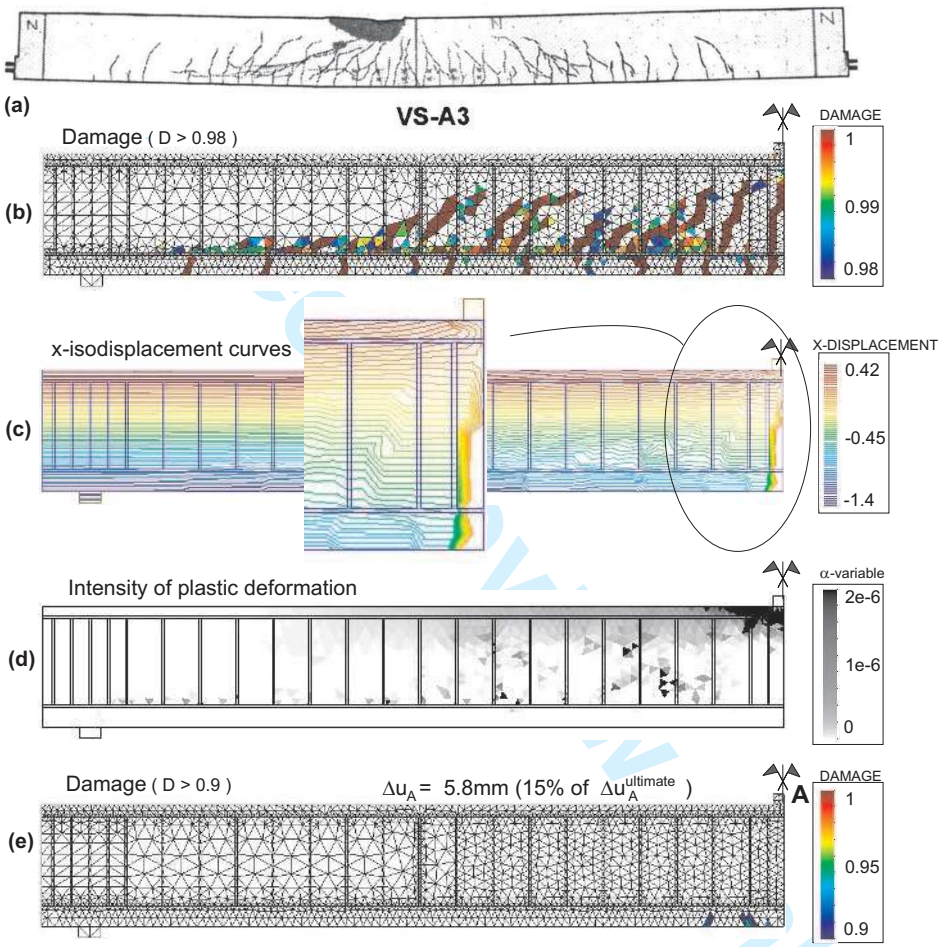

Figure 13: A concrete beam test: (a) experimental result displaying the final distribution of cracks (not well developed) and the upper part concrete crushing in the mid-span of the beam; (b) numerical damage distribution ($d \geq 0.98$) in the end of analysis; (c) iso-horizontal-displacement curves in the end of analysis, displaying the development of a tensile macro-crack in the mid-span of the beam; (d) α-field distribution representing the intensity of the plastic deformations; (e) damage distribution ($d \geq 0.9$) displaying the crack formation initial stage during the loading process and corresponding with a vertical displacement equivalent to the 15% of Δu_A^{ult}.

7 Concluding remarks

In this contribution, a new damage-plastic macroscopic constitutive model for concrete has been presented, validated and its results have been discussed. A remarkable feature is the intrinsic ability to reproduce typical dissimilar responses and failure modes of concrete specimens, depending on the confinement level, such as *"quasi-brittle fracture"* or *"ductile failure"*, even thought the criterion to select the mechanical behavior type is very simple and intuitive.

The model takes advantages of a well established technique, denoted in the paper as *CSDA*, and previously developed by some of the present authors in the context of quasi-brittle material failure in concrete. From the mentioned technology it is possible to simulate many complex damage mechanisms including the nucleation and propagation of multiples tensile cracks, either in highly localized fracture modes (which are typical in plain concrete members) or in a rather distributed fracture patterns (as can be observed in the earliest stages of failure in reinforced concrete structures). An elasto-plastic model has been consistently coupled for capturing the ductile behavior of concrete. The full model simulates, in a computationally efficient way, the transition between a ductile or a quasi-brittle mechanical response. This feature suggests that the model becomes particularly useful in numerical simulations of reinforced concrete structures where both inelastic mechanisms: *(i)* degradation until fracture generation induced by tensile stresses and *(ii)* plasticity with crushing in compression, are present at the moment of the structural collapse.

The model has a reduced number of material parameters, most of them can be obtained from standard laboratory test. This fact, on one hand, facilitates the characterization process, but on the other hand, limits the prediction capability for detailed aspects of the concrete mechanical response. In spite of this, the more relevant phenomenologies have been adequately captured. Thus, in the authors' opinion, the model provides a favorable balance if weighting its simplicity versus its predictability and accuracy.

From the numerical point of view, an efficient integration method has been developed. It is an extension of the *Impl-Ex* strategy, previously proposed by Oliver et al. (2008) (see additional application in Sánchez et al. (2008)). The formulation of such integration scheme improves the performance and robustness of the whole non-linear finite element analysis for problems involving material failure.

Softening for the concrete in the plastic range has not been considered in this work. It is a serious limitation of the present formulation. However, in the authors' opinion, this issue is an open problem in the theoretical modeling of concrete material behavior. The authors think that additional meso-structural information is necessary in order to predict any type of ductile-softening mechanism through an objective and consistent approach. The classical fracture energy concept, widely utilized by engineers as a material parameter for regularizing quasi-brittle response in concrete models, has a questionable physical meaning for compressive regimes.

Acknowledgments

The first, second and fifth author acknowledge financial support from ANPCyT of Argentina through grants PICT 2006-1232, PICT 2008-1228 and from Conicet. Financial support from the Spanish Ministry of Science and Technology trough grant BIA2008-00411 is gratefully acknowledged by the third author.

Appendix I: Thermodynamic admissibility

As a consequence of the dilatant effect (χ-factor) included in the definition of the plastic potential, as also by the absence of the function $\hat{r}(e,\theta)$ in the mathematical expression of $G(\boldsymbol{\sigma},\xi)$, the proposed constitutive model does not belong to the class of *Standard* or *Generalized Associative Materials*. Therefore, some thermodynamic aspects deserve additional analysis. In general, the physical requirements of thermodynamics imply the inclusion of some (mandatory) restrictions limiting the definition range for some materials parameters.

For thermodynamic consistency, it is necessary to guarantee the *Clausius-Duhem Inequality* (from now on simply *CDI*) for arbitrary loading paths. For a purely isothermal process it is expressed as:

$$\mathcal{D}_{mech} = \boldsymbol{\sigma} : \dot{\boldsymbol{\varepsilon}} - \dot{\Psi} \geq 0 \quad \text{(for any loading path)} \tag{48}$$

where $\mathcal{D}_{mech}$ is the mechanical energy dissipation.

Taking in consideration the definitions given in Table 1, and after simple algebraical manipulations on equation (48), the *CDI* can be rewritten as:

$$\mathcal{D}_{mech} = \boldsymbol{\sigma} : \dot{\boldsymbol{\varepsilon}}^p + \frac{\tau_\varepsilon^2}{2}\,\dot{d}(r) - \xi(\alpha)\,\dot{\alpha} \geq 0 \quad \text{(for any loading path)} \tag{49}$$

Since the inelastic mechanisms of damage and plasticity are mutually exclusive, equation (49) implies two different restrictions to be verified for each one of the sub-models respectively, it means:

$$\text{Damage evolution: } \dot{d} > 0\ ;\ \dot{\boldsymbol{\varepsilon}}^p = \dot{\alpha} = 0 \quad ;\quad \textit{CDI} \rightarrow \quad \mathcal{D}_{mech} = \frac{\tau_\varepsilon^2}{2}\,\dot{d}(r) \geq 0 \tag{50}$$

$$\text{Plasticity evolution: } \dot{\alpha} > 0\ ;\ \dot{\boldsymbol{\varepsilon}}^p > 0\ ;\ \dot{d} = 0 \quad ;\quad \textit{CDI} \rightarrow \quad \mathcal{D}_{mech} = \boldsymbol{\sigma} : \dot{\boldsymbol{\varepsilon}}^p - \xi(\alpha)\,\dot{\alpha} \geq 0 \tag{51}$$

For a mechanical process governed by damage evolution, expression (50) can be expanded as:

$$\mathcal{D}_{mech} = \frac{\tau_\varepsilon^2}{2}\,\dot{d}(r) = \left[-H(r)\overbrace{r}^{>0} + \overbrace{q(r)}^{>0} \right] \frac{\overbrace{\dot{r}}^{\geq 0}}{2} \geq 0 \tag{52}$$

$q(r) \in [q_0; 0)$

$r \in [r_0; \infty)$

$\dot{r} = \gamma^d \geq 0$ (in view of the complementary condition, γ^d : damage consistency parameter)

from where it becomes evident that selecting a quasi-brittle material response with strain softening behavior, it means that $H(r) < 0$ (as in the present context), the thermodynamic restriction for positive dissipation is guaranteed for any inelastic process.

For plastic processes, the *CDI* given by the equation (51) reads:

$$\mathcal{D}_{mech} = \boldsymbol{\sigma} : \dot{\boldsymbol{\varepsilon}}^p - \xi(\alpha)\,\dot{\alpha} = \overbrace{\dot{\gamma}^p}^{\geq 0} \left\{ \boldsymbol{\sigma} : \left[\frac{\beta}{2} \|\boldsymbol{S}\|^{\beta-1} \boldsymbol{n} + \chi \frac{\xi(\alpha)}{3} \mathbb{1} \right] + \xi(\alpha)\,\chi\,\sigma_m \right\} \geq 0$$
$$= \underbrace{\frac{\beta}{2} \|\boldsymbol{S}\|^{\beta}}_{\geq 0} + \underbrace{2\,\chi\,\xi(\alpha)\,\sigma_m}_{<0} \geq 0 \tag{53}$$

Taking into account the yielding limit surface, $\psi(\boldsymbol{\sigma}, \xi) = 0$, the norm of the deviator stress tensor can be expressed as:

$$\|\boldsymbol{S}\|^{\beta} = \frac{2\left[k_m - \xi(\alpha)\sigma_m\right]}{\hat{r}(e,\theta)} \tag{54}$$

Then inserting equation (54) into equation (53), a general restriction over the dilatant χ-factor (which assures positive dissipation) can be obtained:

$$\chi \leq \chi_{max} = \overbrace{\frac{\beta}{2\,\hat{r}(e,\theta)}}^{>0} - \overbrace{\frac{\beta\,k_m}{2\,\hat{r}(e,\theta)\,\xi(\alpha)\,\sigma_m}}^{<0} \quad ; \quad \chi \in [0\,;\,\chi_{max}] \tag{55}$$

The constraint given by expression (55) depends on the present stress state and, therefore, it results inadequate as a rational criterion for limiting the maximum value of the material parameter χ. However, a more restrictive upper bound can be obtained for χ by neglecting the second term contribution of the right hand side of equation (55). Note that this assumption is really satisfied for sufficiently large confinement levels, because for any plastic flow state we have: *(i)* k_m = cte (due to $\dot{d} = 0$), *(ii)* β = cte (since it is a material parameter), *(iii)* $\hat{r}(e,\theta) \in [1, \hat{r}_{max}]$ (it means that $\hat{r}(e,\theta)$ is a bounded function) and *(iv)* $\sigma_m \to -\infty$. On the contrary for low triaxiality values ($\sigma_m \to 0$), the second term of the right hand side of equation (55) tends to expand the admissibility range for χ. In view of the previous comments, a very simple inequality can be adopted for practical purposes which guaranties, in any case, the positive energy dissipation:

$$\chi \leq \chi^*_{max} = \frac{\beta}{2\,\hat{r}_{max}} < \chi_{max} \quad ; \quad \chi \in [0\,;\,\chi^*_{max}] \tag{56}$$

where $\hat{r}_{max}$, the maximum value of function $\hat{r}(e,\theta)$, is independent of stress state, and so χ^*_{max}.

Appendix II: Convexity of the damage and plastic limit surfaces

In order to assure uniqueness condition, and due to the model characteristics, the convexity of the plastic or damage surfaces is only required in the separate spaces: $\sigma_m \leq 0$ and $\sigma_m \geq 0$.

The damage limit surface ($\hat{g}(\boldsymbol{\sigma}, q) = 0$) represents an ellipsoid centered in the origin of the Haigh-Westeergard's coordinate system. Consequently, the convexity for the quasi-brittle regime (damage evolution) is assured and no additional restriction for the material data parameters arises.

For the ductile range of the material response, the proper definition of the roundness function $\hat{r}(e, \theta)$ guaranties the convex profile of the yield surface $\psi(\boldsymbol{\sigma}, \xi) = 0$ on any deviatoric plane. A more detailed analysis is necessary to assure the convex profile for variations in the confinement level. In this context, we need to study if the inequality given by:

$$\frac{d^2 \|\boldsymbol{S}\|}{d \sigma_m^2} < 0 \quad ; \quad \text{for } \xi = cte\,;\ \theta = cte\,;\ k_m = cte \tag{57}$$

implies the introduction of any type of restriction over the admissible interval definition for some material parameter. Note that the $\|\boldsymbol{S}\|$ function is obtained from the equation (54). After simple mathematical manipulations on expression (57), and certain simplified assumptions, an upper bound (ω_{max}) arises for the material parameter ω:

$$\omega \leq \omega_{max} = \frac{\xi(\alpha)}{2\, k_m} \quad ; \quad \omega \in [0\,;\, \omega_{max}] \tag{58}$$

In order to obtain full independence with respect to the present stress state, a more restrictive limit value ω^*_{max} can be adopted:

$$\omega \leq \omega^*_{max} = \frac{\xi_{min}}{2\, k_{m\,max}} < \omega_{max} \quad ; \quad \omega \in [0\,;\, \omega^*_{max}] \tag{59}$$

$$\xi_{min} = \xi(\alpha = 0) = \xi_0$$

$$k_{m\,max} = k_m(q = q_0) = \frac{1}{2}\,(2\mu)^{\frac{\beta}{2}}\, q_0^{\beta} \quad \text{(it means undamage material, see eq. (22))}$$

where ξ_0 and q_0 are the initial values for $\xi(\alpha)$ and $q(r)$ respectively, see Section 3.

References

Alfaiate, J., Wells, G., Sluys, L., 2002. On the use of embedded discontinuity elements with crack path continuity for mode-i and mixed-mode fracture. Eng. Fract. Mech. 69, 661–686.

Caballero, A., Lopez, C., Carol, I., 2006. 3-d meso-structural analysis of concrete specimens under uniaxial tension. Comput. Methods Appl. Mech. Engrg. 195, 7182–7195.

Candappa, D., Sanjayan, J., Setunge, S., 2001. Complete triaxial stress-strain curves of high-strength concrete. Journal of Materials in Civil Engineering, ASCE 13, 209–215.

Cervenka, J., Papanikolaou, V., 2008. Three dimensional combined fracture plastic material model for concrete. Int. J. of Plast. 24, 2192–2220.

Contrafatto, L., Cuomo, M., 2006. A framework of elastic-plastic damaging model for concrete under multiaxial stress states. Int. J. of Plast. 22, 2272–2300.

Dahl, K., 1992. Constitutive model for normal and high-strength concrete. Tech. Rep. ABK Report No. R287, Department of Structural Engineering, Technical University of Denmark.

Etse, G., Willam, K., 1994. Fracture energy formulation for inelastic behavior of plain concrete. J. Engng. Mech., ASCE 120, 1983–2011.

Feenstra, P., de Borst, R., 1996. A composite plasticity model for concrete. Int. J. Solids Structures 33, 707–730.

Feist, C., Hofstetter, G., 2006. An embedded strong discontinuity model for cracking of plain concrete. Comp. Meth. Appl. Mech. Eng. 195, 7115–7138.

Gasser, T., Holzapfel, G., 2005. Modeling 3d crack propagation in unreinforced concrete using pufem. Comput. Methods Appl. Mech. Engrg. 194, 2859–2896.

Grassl, P., Jirasek, M., 2006. Damage-plastic model for concrete failure. Int. J. of Solids and Struct. 43, 7166–7196.

Imran, I., 1994. Applications of non-associated plasticity in modeling the mechanical response of concrete. Ph.D. thesis, Dept. of Civil Eng., Toronto University, Canada.

Jirásek, M., 2000. Comparative study on finite elements with embedded discontinuities. Comp. Meth. Appl. Mech. Eng. 188, 307–330.

Kang, H., 1997. A triaxial constitutive model for plain and reinforced concrete behavior. Ph.D. thesis, CEAE Department, University of Colorado, Boulder.

Kang, H., Willam, K., 1999. Localization characteristics of triaxial concrete model. J. Engng. Mech., ASCE, 941–950.

Kang, H., Willam, K., Shing, B., Spacone, E., 2000. Failure analysis of r/c columns using a triaxial concrete model. Computers and Structures 77, 423–440.

Kupfer, H., Gerstle, K., 1973. Behavior of concrete under biaxial stresses. J. Engng. Mech., ASCE 99, 853–866.

Kupfer, H., Hilsdorf, K., Rusch, H., 1969. Behavior of concrete under biaxial stresses. ACI Journal 66, 656–666.

Lemaitre, J., Desmorat, R., 2005. Engineering Damage Mechanics: Ductile, Creep, Fatigue and Brittle Failures. Springer-Verlag, Berlin.

Linero, D., 2006. A model of material failure for reinforced concrete via continuum strong discontinuity approach and mixing theory. Ph.D. thesis, E.T.S. Enginyers de Camins, Canals i Ports, Technical University of Catalonia (UPC), Barcelona, cimne Monograph Nbr.M106.

Lotfi, H., Shing, P., 1995. Embedded representation of fracture in concrete with mixed elements. Int. J. Num. Meth. Eng. 38, 1307–1325.

Lubliner, J., 1990. Plasticity theory. Macmillan Publishing Company, New York.

Luccioni, B., Rougier, V., 2005. A plastic damage approach for confined concrete. Comp. and Structures 83, 2238–2256.

Mattei, N., Mehrabadi, M., Zhu, H., 2007. A micromechanical constitutive model for the behaviour of concrete. Mec. of Materials 39, 367–379.

Meschke, G., Macht, J., Lackner, R., 1998. A damage-plasticity model for concrete accounting for fracture-induced anisotropy. In: deBorst, Bicanic, M. M. (Ed.), Computational Modelling of Concrete Structures,. Balkema, Rotterdam,, pp. 3–12.

Mosler, J., Meschke, G., 2004. Embedded crack vs. smeared crack models: a comparison of elementwise discontinuous crack path approaches with emphasis on mesh bias. Comput. Methods Appl. Mech. Engrg. 193, 3351–3375.

Oliver, J., 2000. On the discrete constitutive models induced by strong discontinuity kinematics and continuum constitutive equations. Int. J. Solids Struct. 37, 7207–7229.

Oliver, J., Huespe, A., Blanco, S., Linero, D., 2005. Stability and robustness issues in numerical modeling of material failure with the strong discontinuity approach. Comput. Meth. App. Mech. Eng. 195 (52), 7093–7114.

Oliver, J., Huespe, A., Sánchez, P., 2006. A comparative study on finite elements for capturing strong discontinuities: e-fem vs x-fem. Comput. Methods Appl. Mech. Engrg. 195(37-40), 4732–4752.

Oliver, J., Huespe, A. E., Cante, J., 2008. An implicit/explicit integration schemes to increase computability of non-linear material and contact/friction problems. Comput. Meth. App. Mech. Eng. 197, 1865–1889.

Oliver, J., Huespe, A. E., Pulido, M. D. G., Chaves, E., 2002. From continuum mechanics to fracture mechanics: the strong discontinuity approach. Engineering Fracture Mechanics 69, 113–136.

Pivonka, P., Ozbolt, J., Lackner, R., Mang, H. A., 2004. Comparative studies of 3d-constitutive models for concrete: application to mixed-mode fracture. Int. J. Numer. Meth. Engng 60, 549–570.

Rudnicki, J., Rice, J., 1975. Condition for the localization of deformations in pressure sensitive dilatant materials. J. Mech. Phys. Solids 23, 371–394.

Sánchez, P. J., Huespe, A. E., Oliver, J., 2008. On some topics for the numerical simulation of ductile fracture. Int. J. Plast. 24, 1008–1038.

Sancho, J., Planas, J., Reyes, D. C. E., Gálvez, J., 2007. An embedded crack model for finite element analysis of concrete fracture. Eng. Fract. Mech. 74, 75–86.

Sfer, D., Carol, I., Gettu, R., Etse, G., 2002. Study of the behavior of concrete under triaxial compression. J. Engng. Mech., ASCE 128, 156–163.

Sánchez, P. J., Huespe, A. E., Oliver, J., Toro, S., 2010. Mesoscopic model to simulate the mechanical behavior of reinforced concrete members affected by corrosion. International Journal of Solids and Structures 47, 559–570.

Vecchio, F., Shim, W., 2004. Experimental and analytical reexamination of classic concrete beam tests. J. of Struct. Eng., ASCE 130, 460–469.

Willam, K., Warnke, E., 1974. Constitutive model for triaxial behaviour of concrete. In: Proc. of Concrete Structures Subj. to triaxial stresses, Inst. Assoc. for Bridges and Struct. Eng., 19, Section III, Zurich. pp. 1–30.

Winkler, B., Hofstetter, G., Lehar, H., 2004. Application of a constitutive model for concrete to the analysis of a precast segmental tunnel lining. Int. J. Num. Anal. Methods in Geomechanics 28, 797–819.

Winkler, B., Hofstetter, G., Niederwanger, G., 2001. Experimental verification of constitutive model for concrete cracking. Proc. Inst. Mech. Eng. 215-Part I, 75–86.